

# Simulating the transport and dispersal of volcanic ash clouds with initial conditions created by a 3D plume model

Zhixuan Cao<sup>1,2</sup> Marcus Bursik<sup>3</sup> Qingyuan Yang<sup>4,5</sup> Abani Patra<sup>\*,1,6</sup>

<sup>1</sup> Mechanical and Aerospace Engineering Department, SUNY Buffalo, Buffalo, NY, USA

<sup>2</sup> Fluids Business Unit, ANSYS Inc, Lebanon, NH, USA

<sup>3</sup> Center for Geohazards Studies, SUNY Buffalo, Buffalo, NY, USA

<sup>4</sup> Earth Observatory of Singapore, Singapore, Singapore

<sup>5</sup> The Asian School of the Environment, Nanyang Technological University, Singapore, Singapore

<sup>6</sup> Data Intensive Studies Center, Tufts University, Medford, MA, USA

Correspondence\*:

Abani Patra

abani.patra@tufts.edu

## 2 ABSTRACT

volcanic ash transport and dispersion (VATD) models simulate atmospheric transport of ash starting from a source originating at the volcano represented by concentration of ash with height. Most VATD models use a source of some prescribed shape calibrated against an empirical expression for the height-mass eruption rate (MER) relation. The actual vertical ash distribution in volcanic plumes usually varies from case to case and has complex dependencies on eruption source parameters and atmospheric conditions. We present here for the first time the use of a three-dimensional (3D) plume model to represent the ash cloud source without any assumption regarding plume geometry. By eliminating assumed behavior associated with a semiempirical plume geometry, the predictive skill of VATD simulations is greatly improved. To date, no VATD simulation adopts initial conditions created from first principles based on a 3D plume simulation. We use our recently developed volcanic plume model based on a 3D smoothed-particle hydrodynamic Lagrangian method, and couple the output to a standard Lagrangian VATD model. We apply the coupled model to the Pinatubo eruption in 1991 to illustrate the effectiveness of the approach. Our investigation reveals that initial particle distribution in the vertical direction has more impact on transport of ash clouds than does the horizontal distribution. Comparison with satellite data indicates that ash particles are concentrated through the depth of the volcanic umbrella cloud, and much lower than the observed maximum plume height.

Keywords: VATD, volcano, 3D plume model, initial conditions, numerical simulation, SPH, Pinatubo, ash transport, ash dispersal

## 1 INTRODUCTION

Volcanic ash, the fine-grained fraction of tephra, can be widely dispersed to synoptic and global scales, and can lead to a degradation of air quality and pose threats to aviation (Tupper et al., 2007). Identification, tracking and modeling the future movement of volcanic ash help route and schedule flights to avoid ash

24 clouds. Numerical estimation of ash distribution using known and forecast wind fields is necessary if we  
25 are to accurately predict ash cloud propagation and spread. Numerous VATD models have been developed  
26 by both civil and military aviation, and meteorological agencies to provide forecasts of ash cloud motion  
27 (Witham et al., 2007), such as Puff (Tanaka, 1991; Searcy et al., 1998), VAFTAD (Heffter and Stunder,  
28 1993), Tephra (Bonadonna et al., 2005), HYSPLIT(Stein et al., 2015; Rolph et al., 2017) and Ash3d  
29 (Schwaiger et al., 2012). New techniques have been integrated into VATDs to satisfy increasing demands  
30 for different types of output, model accuracy and forecast reliability. This contribution explores a method  
31 for creating initial conditions for VATD simulations, which promises to reduce user inversion and hence  
32 improve prediction capability.

33 Fero et al. (2009) and Stohl et al. (2011) showed that initial source conditions have significant effects on  
34 simulation of volcanic ash transport. Constantinescu et al. (2021) proved that an enhanced initial condition  
35 provides an overall better fit of the deposit than models without a disk source, demonstrating the significant  
36 impact of initial condition on ash dispersion. Besides location of the eruption vent and timings of the release,  
37 traditional VATD simulation requires key global descriptors of the volcanic plume, especially plume height,  
38 grain size, eruption duration and mass loading, or alternatively, a mass eruption rate (MER). No matter  
39 how these global descriptors are obtained, they are used to furnish the initial conditions for VATDs in the  
40 form of a line-source term of a spatio-temporal distribution of particle mass. It is a common practice to  
41 pick values for these global descriptors using an empirical expression for the height-MER relation. The  
42 values for the descriptors can also be found by parameter calibration (e.g. Fero et al., 2008, 2009; Stohl  
43 et al., 2011; Zidikheri et al., 2017). One-dimensional (1D) plume models serve as an alternative option to  
44 provide these values. For example, Bursik et al. (2012) used the 1D model puffin (Bursik, 2001) to generate  
45 estimates of mass eruption rate and grain size. In some cases, an extra step is adopted to spread ash particles  
46 from the line source horizontally, resulting in an initial ash cloud in 3D space. The horizontal spreading  
47 depends on an empirical expression as well. For example, the VATD model Puff spreads particles from the  
48 line source uniformly in the horizontal direction within a given radius. Considering the complexities of  
49 volcanic eruptions, the actual ash distribution in the initial ash cloud should vary from case to case and with  
50 time, making it difficult to find one general expression that is suitable for all cases. It is useful therefore to  
51 investigate alternative ways for creating initial ash clouds without assumptions regarding plume geometry,  
52 or numerical inversion. This provides the major motivation of this paper.

53 VATD models can be categorized into Lagrangian particle tracking and Eulerian advection-diffusion types.  
54 Among several available particle tracking models, such as, Hypact (Walko et al., 1995), Puff (Searcy et al.,  
55 1998), CANERM (D'amus, 1998), and HYSPLIT (Draxler and Hess, 1998) and advection-diffusion  
56 models, such as, Tephra (Bonadonna and Houghton, 2005), Fall3D (Folch et al., 2009), and Ash3D  
57 (Schwaiger et al., 2012), we adopt a particle tracking model, Puff, as the primary VATD model. Puff  
58 can accept a 3D point cloud description of the starting ash cloud as an initial condition, which makes  
59 it technically easier to couple with 3D plume models. Puff initializes a discrete number of tracers that  
60 represent a sample of the eruption cloud, and calculates transport, turbulent dispersion, and fallout for  
61 each representative tracer. A cylinder emanating vertically from the volcano summit to a specified plume  
62 height is the standard approach to provide a simple model of the geometry of a typical ash column. Puff  
63 minimally requires horizontal wind field data. The “restart” feature of Puff makes it technically feasible to  
64 accommodate the hand-off between a plume simulation and the Puff simulation in terms of time and length  
65 scales. We also use the Hybrid Single-Particle Lagrangian Integrated Trajectory model (HYSPLIT) (Stein  
66 et al., 2015; Rolph et al., 2017) to better understand simulation results from Puff in this study.

67 Besides parameter calibration, 1D plume models have been used to obtain global descriptors of volcanic  
68 plumes. 1D plume models (e.g. Woods, 1988; Bursik, 2001; Mastin, 2007; de'Michieli Vitturi et al., 2015;  
69 Folch et al., 2016; Pouget et al., 2016b) solve the equations of motion in 1D using simplifying assumptions,  
70 and hence depend on estimation of certain parameters, especially those related to the entrainment of air,  
71 which is evaluated based on two coefficients: a coefficient due to turbulence in the rising buoyant jet, and  
72 one due to the crosswind field. Different 1D models adopt different entrainment coefficients based on a  
73 specific formulation or calibration against well-documented case studies. The feedback from plume to  
74 atmosphere is usually ignored in 1D models. While these 1D models generated well-matched results with  
75 3D models for plumes that are dominated by wind (often called weak plumes) much greater variability  
76 is observed for strong plume scenarios (Bursik et al., 2009; Costa et al., 2016). On the other hand, 3D  
77 numerical models for volcanic plumes based on first principles and having few parametrized coefficients  
78 (Oberhuber et al., 1998; Neri et al., 2003; Suzuki et al., 2005; Cerminara et al., 2016a; Cao et al., 2018)  
79 naturally create a 3D ash cloud, which could serve directly as an initial state of the volcanic material for  
80 VATDs. However, there is no VATD simulation using such 3D ash clouds as initial conditions. In this paper,  
81 we will carry out VATD simulations using an initial state for the ash cloud based on 3D plume simulations,  
82 generated with Plume-SPH (Cao et al., 2018, 2017). The implementation techniques described in this paper  
83 can be applied to any combination of VATD model and 3D plume model even though our investigation is  
84 based on a specific VATD model and plume model.

85 The 1991 eruption of Pinatubo volcano is used as a case study. Pinatubo erupted between June 12 and 16,  
86 1991, after weeks of precursory activity. The climactic phase started on June 15 at 0441 UTC and ended  
87 around 1341 UTC (Holasek et al., 1996a). The climactic phase generated voluminous pyroclastic flows,  
88 and sent Plinian and co-ignimbrite ash and gas columns to great altitudes (Scott et al., 1996). The evolution  
89 of the Pinatubo ash and SO<sub>2</sub>louds was tracked using visible (Holasek et al., 1996a), ultraviolet (Total  
90 Ozone Mapping Spectrometer; TOMS) (Guo et al., 2004a) and infrared sensors, including the Advanced  
91 Very High-Resolution Radiometer (AVHRR) (Guo et al., 2004b). There is sufficient observational data to  
92 estimate the eruption conditions for the climactic phase of the eruption (Suzuki and Koyaguchi, 2009). The  
93 availability of calibrated eruption conditions and extensive observational data regarding ash cloud transport  
94 make the Pinatubo eruption an ideal case study.

## 2 MATERIALS AND METHODS

### 95 2.1 Plume-SPH Model

96 Plume-SPH (Cao et al., 2018) is designed to describe an injection of well mixed solid and volcanic gas  
97 from a circular vent above a flat surface into a stratified stationary atmosphere. The basic assumptions of  
98 the model are:

- 99 1. Molecular viscosity and heat conduction is neglected since turbulent energy and momentum exchange  
100 are dominant.
- 101 2. Erupted material consisting of solid with different size and mixture of gases is assumed to be well  
102 mixed and behave like a single phase fluid (phase 2) which is valid for eruptions with fine particles and  
103 ash.
- 104 3. Air, which is assumed to be a well mixed mixture of different gases, is assumed to be another phase  
105 (phase 1).
- 106 4. Assume thermodynamic equilibrium and dynamic equilibrium between the two phases. As a result,  
107 both phases share the common energy equation and momentum equations.

- 108 5. All other microphysical processes (such as the phase changes of H<sub>2</sub>O aggregation, disaggregation,  
 109 absorption of gas on the surface of solids, solution of gas into a liquid) and chemical processes are not  
 110 considered in this model.  
 111 6. The effect of wind is also not yet considered in this model.

Based on above assumptions, the governing equations of our model are given as:

$$\frac{\partial \rho}{\partial t} + \nabla \cdot (\rho \mathbf{v}) = 0 \quad (1)$$

$$\frac{\partial \rho \xi}{\partial t} + \nabla \cdot (\rho \xi \mathbf{v}) = 0 \quad (2)$$

$$\frac{\partial \rho \mathbf{v}}{\partial t} + \nabla \cdot (\rho \mathbf{v} \mathbf{v} + p \mathbf{I}) = \rho \mathbf{g} \quad (3)$$

$$\frac{\partial \rho E}{\partial t} + \nabla \cdot [(\rho E + p) \mathbf{v}] = \rho \mathbf{g} \cdot \mathbf{v} \quad (4)$$

112 where  $\rho$  is the density,  $\mathbf{v}$  is the velocity,  $\xi$  is the mass fraction of ejected material,  $\mathbf{g}$  is the gravitational  
 113 acceleration,  $\mathbf{I}$  is a unit tensor.  $E = e + K$  is the total energy which is a summation of kinetic energy  $K$   
 114 and internal energy  $e$ . An additional equation is required to close the system. In this model, the equation  
 115 for closing the system is the following equation of state (EOS).

$$p = (\gamma_m - 1) \rho e \quad (5)$$

116 where

$$\gamma_m = R_m / C_{vm} + 1 \quad (6)$$

$$R_m = \xi_g R_g + \xi_a R_a \quad (7)$$

$$C_{vm} = \xi_s C_{vs} + \xi_g C_{vg} + \xi_a C_{va} \quad (8)$$

$$\xi_a = 1 - \xi \quad (9)$$

$$\xi_g = \xi \cdot \xi_{g0} \quad (10)$$

$$\xi_s = \xi - \xi_g \quad (11)$$

122 where,  $C_v$  is the specific heat with constant volume,  $R$  is the gas constant.  $\xi$  is the mass fraction of erupted  
 123 material. The subscript  $m$  represents mixture of ejected material and air,  $s$  represents solid portion in the  
 124 ejected material,  $g$  represents gas portion in the ejected material,  $a$  represents air,  $0$  represents physical  
 125 properties of erupted material.  $\xi_{g0}$  is the mass fraction of vapor in the erupted material.

126 Three different boundary conditions are applied in this model. At the vent, temperature of erupted  
 127 material  $T$ , eruption velocity  $\mathbf{v}$ , the mass fraction of vapor in erupted material  $\xi_{g0}$  and mass discharge  
 128 rate  $\dot{M}$  are given. The pressure of erupted material  $p$  is assumed to be the same as ambient pressure for  
 129 pressure-balanced eruption. The radius of the vent is determined from  $\rho$ ,  $\dot{M}$  and  $\mathbf{v}$ . Non-slip wall boundary  
 130 condition is applied to the flat ground, where we enforce the velocity to be zero. With further assumption  
 131 that the ground is adiabatic, internal energy flux, which consists of heat flux and energy flux carried by  
 132 mass flux, vanishes on the wall boundary. Pressure outlet boundary condition is applied to the surrounding  
 133 atmosphere where the pressure is given. Except for the pressure, boundary values for density, velocity, and

134 energy are determined by numerical calculation naturally. The initial condition for Plume-SPH is created  
 135 based on the atmosphere profile before the eruption.

136 The governing equations, EOS, boundary conditions, and initial conditions establish a complete mathematical  
 137 model. The model is then discretized using smoothed particle hydrodynamics (SPH) method (Gingold  
 138 and Monaghan, 1977). The computational domain is discretized by SPH particles. The current version,  
 139 Plume-SPH (Cao et al., 2018) uses two types of SPH particles: 1) particles of phase 1 to represent ambient  
 140 air, and 2) particles of phase 2 to represent erupted material. So before the eruption, the computational  
 141 domain is fully occupied by particles of phase 1. During the eruption, particles of phase 2 are injected  
 142 into the computational domain. The discretized model is then converted into computational software  
 143 (Plume-SPH) based on a parallel data management framework (Cao et al., 2017).

144 The input parameters for Plume-SPH include the eruption condition at vent, the material properties, and  
 145 atmosphere profile. The eruption parameters, material properties and atmosphere for the “Strong plume–no  
 146 wind” case in the recent comparison study on eruptive column models (Costa et al., 2016) are adopted.  
 147 Eruption conditions and material properties are listed in Table 1. Note that the density of erupted material  
 148 at the vent and radius of the vent can be computed from the given parameters. The eruption pressure  
 149 is assumed to be the same as the atmospheric pressure at the vent, hence is not given in the table. The  
 150 vertical profiles of atmospheric properties were based on the reanalysis data from European Centre for  
 151 Medium-Range Weather Forecasts (ECMWF) for the period corresponding to the climactic phase of the  
 152 Pinatubo eruption.

153 Running of Plume-SPH essentially updates physics quantities, such as temperature, velocity, and the  
 154 position of SPH particles in each time step. During Plume-SPH simulation, SPH particles of phase 2,  
 155 which represent the erupted material, are injected from the eruption vent into the computation domain with  
 156 an initial injection velocity. As they move upwards, these particles will get mixed with SPH particles of  
 157 phase 1, which represent the air, during the whole simulation. Their physics quantities get updated as well.  
 158 After the simulation, the computation domain will be filled with SPH particles of both phase 1 and phase 2.  
 159 Removing all SPH particles of phase 1 from the computation domain, all of the left SPH particles are these  
 160 particles that represent the erupted material, which naturally forms a plume (see Fig. 1).

## 161 2.2 Puff and Initial Ash Cloud

162 Puff (Tanaka, 1991; Searcy et al., 1998) is a dynamic pollutant tracer model. The model is based on a 3D  
 163 Lagrangian form of the fluid mechanics, in which the material transport is represented by the fluid motion,  
 164 and diffusion is parameterized by a stochastic process of random walk. Here, the model is constructed by a  
 165 sufficiently large number of Lagrangian tracer particles with a random variables  $\mathbf{R}_i(t) = (x(t), y(t), z(t))$ ,  
 166 where  $i = 1 \sim M$ , which represent position vectors of particles from the origin of the ash source at the  
 167 time  $t$ .  $M$  is the total number of Lagrangian tracer particles, a sample of all the ash particles.

$$\mathbf{R}_i(t + \Delta t) = \mathbf{R}_i(t) + \mathbf{W}(t)\Delta t + \mathbf{Z}(t)\Delta t + \mathbf{S}_i(t)\Delta t \quad (12)$$

168 Here,  $\mathbf{W}$  accounts for local wind advection,  $\mathbf{Z}$  is generated by Gaussian random numbers and accounts  
 169 for turbulent dispersion, and  $\mathbf{S}$  is the terminal gravitational fallout velocity or settling speed, which depends  
 170 on a tracer’s size.

171 To start a Puff simulation, it requires a collection of tracer particles as the initial condition. The tracer  
 172 particles have three basic properties, age, size and position. The age of each particle is the elapsed time  
 173 from when they were released from the site. Ash particles in the initial ash cloud have zero ages. Ash

size distribution is initialized using a Gaussian shape on a logarithmic scale. According to the mean and standard deviation provided by the user, Puff assigns size to each particle. Puff initializes the position of each particle according to semiempirical expressions. The height of each particle is determined according to the specified distribution from the surface (1000 mbar  $\cong$  0 m) to the top of the plume height,  $H_{max}$ , which is given by the user. Puff also supports reading predefined initial ash clouds from a file, containing the coordinates of all tracer particles.

The commonly used vertical particle distribution in Puff is the Poisson distribution. For the Poisson distribution, the vertical height of ash particles is given by Eq. (13):

$$H = H_{max} - 0.5H_{width}P + H_{width}R \quad (13)$$

where  $P$  is an integral value drawn from a Poisson distribution of unit mean,  $R$  is a uniformly distributed random number between 0 and 1,  $H_{max}$  is the maximum plume height,  $H_{width}$  represents an approximate vertical range over which the ash will be distributed. So for Poisson distribution, the user can specify two parameters,  $H_{max}$  and  $H_{width}$ . Another commonly used vertical ash distribution in VATD simulation is Suzuki. For the Suzuki plume shape (Suzuki et al., 1983), the ash mass vertical distribution is assumed to follow the Eq. (Eq. (14)):

$$Q(z) = Q_m \frac{k^2(1 - z/H_{max})\exp(k(z/H_{max} - 1))}{H_{max} [1 - (1 + k)\exp(-k)]} \quad (14)$$

Where  $Q_m$  is the total mass of erupted material,  $k$  is shape factor, which is an adjustable constant that controls ash distribution with height. A low value of  $k$  gives a roughly uniform distribution of mass with elevation, while high values of  $k$  concentrate mass near the plume top. So for Suzuki distribution, besides the plume height  $H_{max}$ , there is another user specified parameter,  $k$ .

Puff initializes the horizontal distribution of ash particles according to semiempirical expression as well. Puff uses a uniformly distributed random process to determine ash particle locations in a circle centered on the volcano site. The maximum radius (at plume top) at which a particle can be located is given as “horizontal spread”. The horizontal displacement from a vertical line above the volcano is a random value within a circle of which the radius equals the “horizontal spread” multiplied by the ratio of the particle height  $H$  to the maximum  $H_{max}$ , see Eq. 15. So the resulting shape of the particle distribution within the plume is an inverted cone in which particles are located directly over the volcano at the lowest level and extend out further horizontally with increasing plume height.

$$r(H) = r_{max}H/H_{max}R \quad (15)$$

where  $r(H)$  is the radius of the horizontal circle, within which all particles at the height of  $H$  are located.  $r_{max}$  is the horizontal spread.  $H$  is the height,  $R$  is an uniformly distributed random number between 0 and 1.

In summary, particle distributions in the initial ash cloud generated by semiempirical expressions are controlled by several parameters, for example,  $H_{max}$ ,  $H_{width}$ , and  $r_{max}$  if the user choose to use semiempirical expressions Eq. (13) and (15). Users can optimize or calibrate these parameters to adjust the initial condition for Puff so that the simulated results match better with observations. Besides the initial ash cloud, other input parameters for Puff are diffusivity in the vertical and horizontal directions, start and end time of the eruption, and eruption duration. When creating initial conditions from output of Plume-SPH,

209 the total number of Lagrangian tracers is the count of all SPH particles of phase 2 in the plume. The same  
210 total number of Lagrangian tracers are used when creating the initial ash cloud based on semiempirical  
211 expressions. All input parameters for Puff are listed in Table 2.

### 212 **2.3 Creation of Initial Ash Cloud From Plume-SPH Output**

213 In this study, we convert the output of Plume-SPH into initial ash cloud which serves as the initial  
214 condition for Puff. The method proposed consists in generating the initial ash cloud directly from Plume-  
215 SPH, foregoing assumptions and estimates, or inverse modeling, regarding ash injection height and timing.  
216 The steps to create an initial ash cloud based on the raw output of Plume-SPH are shown in Fig. 1. The  
217 initial ash cloud is created from SPH particles of phase 2, which represents the erupted material in the  
218 model. After reaching the maximum rise height and starting to spread horizontally, particles of phase 2  
219 form an initial umbrella cloud (Fig. 2). The 3D plume simulation is considered complete once the umbrella  
220 cloud begins to form. Parcels that will be transported by the ambient wind are those above the “corner”  
221 region, where mean plume motion is horizontal rather than vertical. With such consideration, we introduce  
222 an elevation threshold, which is the lower elevation limit of the ash that will be transported by the VATD.  
223 All SPH particles with elevation lower than the threshold are excluded when creating the initial ash cloud.  
224 The inflection point from vertical raising to horizontal spreading happens around 15 km according to the  
225 averaged vertical velocity ((d) in Fig. 2) and horizontal velocity ((e) in Fig. 2)). Below this inflection  
226 point, particle trajectories are primarily vertical in the stalk-like eruption column. Above this level, particle  
227 trajectories are primarily horizontal, as they flow into the umbrella cloud gravity current. So we choose 15  
228 km to be the elevation threshold in this study.

229 Considering that SPH particles are only discretization points, each is assigned a grain size according to a  
230 given total grain size distribution (TGSD) (Paladio-Melosantos et al., 1996), and a concentration according  
231 to the mass and volumetric eruption rate. The Plume-SPH discretization points are thus switched to Puff  
232 Lagrangian tracer particles having grain sizes and concentrations. The coordinates of these tracer particles,  
233 which are initially in the local Cartesian coordinate system of Plume-SPH, are converted into Puff’s global  
234 coordinate system, which is given in terms of (*longitude, latitude, height*). Puff takes the initial ash  
235 cloud, consisting of the collection of Lagrangian tracer particles with grain size and concentration, and  
236 propagates from time  $t$  to time  $t + \Delta t$  via solution to an advection/diffusion equation (Eq. (12)).

237 To summarize, there are four steps to create an initial ash cloud from the raw output of Plume-SPH:

- 238 1. filter by SPH particle type to select SPH particles that represent erupted material (phase 2)
- 239 2. filter by a mean velocity threshold to select the upper part (above the “corner” region) dominated by  
240 horizontal transport
- 241 3. switch SPH discretization points to Lagrangian tracer particles, by assigning grain size to each particle
- 242 4. convert coordinates of the SPH Lagrangian tracers into the VATDs’ geographic coordinate system

243 The features of the volcanic plume and resulting initial ash cloud used in the case study are shown in Fig. 2.  
244 It is important to point out that since both Plume-SPH and Puff are based on the Lagrangian method, there  
245 is no extra step of conversion between an Eulerian grid and Lagrangian particles.

### 246 **2.4 Puff Restart**

247 The plume and ash transport models are run at different time scales and length scales. The spatial and  
248 temporal resolutions of the plume simulations are much finer than those of the ash transport model. It takes  
249 tens of minutes (600 s in this case) for the Pinatubo plume to reach a steady height. However the eruption  
250 persisted for a few hours (9 hours for the climactic phase of Pinatubo eruption), and it may be necessary

251 to track ash transport for days following an eruption. At present, it is too computationally expensive to  
252 run 3D plume simulations of several hours in real time. In order to handle the difference in time scale, we  
253 mimic a continuing eruption with intermittent pulses releasing ash particles. In particular, we restart Puff at  
254 an interval of 600 s, i.e., the physical time of the plume simulation to reach a steady height. At every Puff  
255 restart, we integrate the output of the last Puff simulation and Plume-SPH into a new ash cloud. This new  
256 ash cloud serves as a new initial condition with which to restart a Puff simulation. A sketch demonstrating  
257 the overall restart process is shown in Fig. (3). The total number of Lagrangian tracer particles used in Puff  
258 thus equals the summed number of particles in all releases. The total number of tracer particles is therefore  
259 no longer a user-selected parameter. Fero et al. (2008) proposed using more realistic time-dependent plume  
260 heights. We do not adopt that strategy here for simplicity, although the idea would be straightforward in  
261 execution, given time-dependent eruption conditions.

### 3 RESULTS

262 Transport of volcanic ash resulting from the Pinatubo eruption on June 15, 1991, is simulated using two  
263 different initial conditions. The first type of initial condition is created in a traditional way according to  
264 user specified parameters ( $H_{max}$ ,  $H_{width}$  and  $r_{max}$ ) and the semiempirical plume shape expressions (Eq. (13) and (15)). We use the observed plume height (40 km) as  $H_{max}$  and adopt two other parameters from previous study(Fero et al., 2008). The second type of initial condition is created by the new method proposed in this paper. To create initial conditions using the new method described in this paper, the plume rise is simulated first by Plume-SPH. Then the initial ash cloud is obtained by processing the raw output of Plume-SPH following steps described in Sec. 2.3. Except for initial conditions, the simulation parameters that control the VATD simulation are the same for both simulations. Simulated ash transport results are compared against observations.

272 The simulation results using different initial conditions are compared with TOMS images and AVHRR  
273 BTD ash cloud map imagery (Fig. 4). The Puff simulation results are post-processed by the following steps  
274 to calculate the relative concentration.

- 275 1. The 3D computational domain is discretized into a collection of cells (latitude, longitude, elevation),  
276 each cell is of size 0.2 degree x 0.2 degree x 1 km
- 277 2. Find the cell that has maximum number of particles (tracer particle), let's say the maximum number of  
278 particles is  $N_{max}$ .
- 279 3. Exclude all cells that has number of particles less than 5.
- 280 4. Calculate the relative concentration of each cell by dividing the number of particles in the cell by  
281  $N_{max}$ .

282 In the contour, we plot the relative concentration of the cell that has maximum number of particles at a given  
283 (*latitude*, *longitude*). In addition to the relative concentration, we also plot the contours of maximum  
284 height of the ash cloud (Fig. 5), which is obtained by the following post-processing steps.

- 285 1. The 3D computational domain is discretized into a collection of cells (latitude, longitude, elevation),  
286 each cell is of size 0.2 degree x 0.2 degree x 1 km
- 287 2. Exclude all cells that have number of particles less than 5.
- 288 3. The maximum height is the cell center height of the top cell among all cells with the same  
289 (*latitude*, *longitude*).

290 We also calculated the Figure of Merit in Space (FMS) according to the definition: FMS = (area of  
291 intersection of Puff forecast footprint and satellite image extent)/(area of union).

292 The differences between simulated ash transport by the “Semiempirical initial cloud + Puff” and “Plume-  
293 SPH+ Puff” conditions are significant. We first check the maximum relative concentration in Fig. 4. At  
294 23 hours and 31 hours after the beginning of the climactic phase, the simulated ash concentration based  
295 on the initial conditions created from Plume-SPH is obviously closer to observation than that based on  
296 the initial condition generated from semiempirical expressions, especially in terms of the location where  
297 the high concentration ash locate. This is confirmed by the FMS, which is 0.249 (23 hours) and 0.269  
298 (31 hours) for Plume-SPH results while 0.063 (23 hours) and 0.065 (31 hours) for semiempirical initial  
299 clouds. Around 55 hours after the beginning of the climactic phase, the disparity between observation and  
300 simulation becomes more obvious. Ash in the “Semiempirical initial cloud + Puff” simulation is located far  
301 west of the observation, with a FMS value equal to 0.058. The high concentration area of the “Plume-SPH  
302 + Puff” simulation, even though closer to observation, has also propagated further down the wind direction  
303 than the observation with the FMS goes down to 0.085.

304 Then check the maximum cloud height in Fig. 5 together with the wind field indicated in HYSPLIT  
305 forward trajectory tracking, which starts at 1624 UTC on June 15 (see Fig. 6). One interesting observation  
306 is that the ash cloud is transporting, at least, in two separate layers (directions) independently. From Fig. 6,  
307 we can see that the wind between elevations of 10 km and 15 km blew from north-east to south-west, while  
308 winds of higher elevation blew from east to west. The directions of wind naturally separate the ash cloud  
309 into two layers. In the “Semiempirical initial cloud + Puff” results, the lower elevation layer is missing,  
310 which is the major contribution to the big differences between these two simulation results in Fig. 4. Even  
311 for the upper layer, the maximum cloud height of “Semiempirical initial cloud + Puff” simulation results is  
312 higher than that of “Plume-SPH+ Puff” results. Such differences can not be captured by metrics based on  
313 footprint, such as FMS. At 55 hours after the eruption, the observed high concentration ash, which is at a  
314 relatively lower elevation (inferred from the wind direction at different elevations in Fig. 6 and the eruption  
315 location), is missing in the “Plume-SPH + Puff ” simulation results. This leads to a big decrease of FMS  
316 values from 0.269 to 0.085. One possibility is that these ashes are from eruptions after the climactic phase.  
317 In our current simulation, we use the eruption condition for the climactic phase generating plume height  
318 for the climactic phase, but satellites see ashes from all eruption phases.

319 The only difference between these two simulations is the initial distribution of ash parcels. The main  
320 difference between simulation results from the “Plume-SPH + Puff” and the “Semiempirical initial cloud +  
321 Puff” runs can be directly attributed to the initial ash particle distribution, which we discuss further in the  
322 following section.

### 323 3.1 Effect of plume height ( $H_{max}$ )

324 In this section, we discuss the vertical distribution of ash particles in the initial ash cloud. The majority  
325 of volcanic ash particles are usually injected at an elevation lower than the plume height. For instance,  
326 Holasek et al. (1996a,b) reported the maximum Pinatubo plume height as  $\sim 39$  km while the cloud heights  
327 were estimated at  $\sim 20 - 25$  km. Self et al. (1996) reported that the maximum plume height could have  
328 been  $> 35$  km, but that plume heights were  $23 \sim 28$  km after  $\sim 15 - 16$  hours. The neutral buoyancy  
329 height of the Pinatubo aerosol cloud was estimated with different methods at:  $\sim 17 - 26$  km (lidar) by  
330 DeFoor et al. (1992),  $\sim 20 - 23$  km (balloon) by Deshler et al. (1992),  $\sim 17 - 28$  km (lidar) by Jäger (1992),  
331 and  $\sim 17 - 25$  km (lidar) by Avdyushin et al. (1993). Based on comparison between simulated clouds  
332 with early infrared satellite imagery of Pinatubo, Fero et al. (2008) reported that the majority of ash was  
333 transported between 16 km and 18 km. These observations make good physical sense, as particles are

334 concentrated near the intrusion height of the umbrella cloud, not near the plume top, because the plume top  
335 is due to momentum overshoot. However, the empirical expressions for the height-MER relation, which  
336 are commonly adopted to create initial conditions for VATD simulations, tend to place the majority of ash  
337 particles closer to the top if one uses observed plume height in the empirical expressions.

338 Here we investigate two commonly used plume shapes, the Poisson (see Eq. (13)) and Suzuki (see Eq.  
339 (14)). Particle distributions (in terms of mass percentage or particle number percentage) in the vertical  
340 direction in the initial ash cloud are shown in Fig. 7. In that figure, the vertical particle distribution based on  
341 Plume-SPH output is compared with the vertical particle distribution created based on semiempirical shape  
342 expressions. Both Poisson and Suzuki distributions in Fig. 7 takes  $H_{max} = 40$  km, which is close to the  
343 reported observation of plume height. When adopting the Poisson distribution, see (c) in Fig. 7, the majority  
344 of the particles are between 30 km ~ 40 km. Obviously, the Poisson function distributes the majority of ash  
345 at a higher elevation than was observed (e.g. Fero et al., 2008). As for the Suzuki distribution, (d) in Fig. 7,  
346 the majority of ash particles also occur in a range that is significantly higher than 25 km. Note that in the  
347 plot (d), the Suzuki constant  $k$  is set to 4, which is commonly used for sub-plinian and plinian eruption  
348 columns (Pfeiffer et al., 2005). As for initial ash clouds based on Plume-SPH simulation, most ash particles  
349 are distributed between ~ 17 - 28 km, which matches well with observations. The plume height is also  
350 consistent with observation.

351 For the Poisson distributions, the ash particles cannot be lower without changing the plume height. To  
352 distribute the majority of ash particles at a lower elevation, the plume height must be reduced to a value  
353 smaller than the observed plume height. Adjusting parameters such as plume height in the empirical  
354 expression is actually the traditional source term calibration method. A set of initial ash clouds using  
355 different plume heights based on the Poisson distribution is shown in Fig. 8. The plume heights adopted in  
356 plume shape expressions are not obtained from any plume model or observation of plume height, but by  
357 *a posteriori* calibration to later-observed ash cloud transport heights. For Suzuki distribution, adjusting  
358 the Suzuki constant can adjust the distribution of ash particles in vertical direction. As shown in Fig. 7,  
359 when  $k$  is equal to 1 (see (e)), the majority of ash particles are at a lower elevation than observation. With  
360  $k = 3$  and  $k = 6$  (figure (g) and (h)), the majority of ash particles are at a higher elevation than observation.  
361 When  $k$  is set to 2 (see (f)), we can see that the majority of ash particles are roughly distributed in the range  
362 17 - 28 km. But the shape does not look like a typical plume, as particles are more uniformly distributed in  
363 the vertical direction. In addition, the “best fit” Suzuki constant is different from the typical value, which  
364 is 4 (Pfeiffer et al., 2005), for sub-plinian and plinian eruptions, meaning that we can not apply previous  
365 experiences into the semiempirical expression for this eruption.

366 The ash clouds created by the Poisson distribution with different plume heights are used as initial  
367 conditions in Puff simulations, whose results are shown in Fig. 11. Except for the plume height, all other  
368 parameters for creating an initial ash cloud are the same as those in Table 2. Of course, the range over which  
369 the majority of ash particles is located is lower when using lower plume heights. Figure 11 thus shows that  
370 the plume height has a significant influence on the ash transport simulation. The maximum heights of the  
371 simulated ash cloud are completely different when using different  $H_{max}$  values in the Poisson expression.  
372 When the plume height is 10 km, the ash lags behind that observed and its FMS is 0.055, which is very  
373 close to FMS when  $H_{max}$  is 40 km. For the cases that  $H_{max}$  is 20 km and 30 km, the FMS values are 0.121  
374 and 0.142 respectively. Taking 20 km as the plume height better represents the lower elevation portion of  
375 the ash cloud, while taking 30 km as the plume height better represents the higher elevation portion of the  
376 ash cloud.

377    Simulation results based on a calibrated plume height of 30 km show a footprint similar to those of  
378    “Plume-SPH + Puff”, although smaller in terms of area. However, the initial ash cloud created by a Poisson  
379    distribution with a plume height around 35 km generates the best match ash with observation in terms of  
380    FMS metric, with the FMS value reaching 0.227. That is to say, a plume height lower than the real plume  
381    height is required by the Poisson plume shape to distribute ash particles at elevations comparable to the  
382    “true” ash distribution. Even for the best matched results, the high concentration area does not match with  
383    observation well.

384    It is clear that the initial condition of vertical ash distribution has dominant effect on VATD simulation,  
385    so it is critical for the forecast capability of VATD simulations to explore more accurate and adaptive ways  
386    for establishing the initial ash distribution, especially methods that do not rely on *a posteriori* parameter  
387    calibration or inversion.

### 388    3.2 Effect of Vertical Spread ( $H_{width}$ )

389    In the previous section, we explored the effects of adjusting the plume height to change the vertical  
390    ash distribution at the source. In this section, we investigate the importance of another parameter in the  
391    semiempirical Poisson expression (Eq. (13)). We vary the “vertical spread”,  $H_{width}$ , in the range  $\sim 3 - 10$  km.  
392    A set of initial ash clouds with different vertical spreads are shown in Fig. 8. Except for vertical  
393    spread, all other parameters for creating an initial ash cloud are the same as those in Table 2. The vertical  
394    range within which the majority of ash particles are located becomes narrower when a smaller value for the  
395    vertical spread parameter is used. The ash clouds based on different vertical spread parameters are then  
396    used as initial conditions in Puff simulations.

397    The VATD results are shown in Fig. 11. Adjusting the vertical spread changes particle distribution in  
398    the vertical direction, and thus, not surprisingly, affects the VATD simulation results. None of the VATD  
399    simulations based on initial ash clouds with vertical spreads equal to 3 km or 5 km yield better results than  
400    do VATD simulations based on initial conditions created by Plume-SPH (see Fig. 11). But when we take  
401    10 km as the vertical spread, we get a FMS that is very close to Plume-SPH, even though the shape of the  
402    ash cloud footprint and the maximum height of the ash cloud are completely different.

403    The calibration tests on vertical spread, carried out here, are certainly not exhaustive. One could do a more  
404    comprehensive calibration throughout the multi-dimensional parameter space (for Poisson distribution,  
405    the parameter space is two dimensional) and find better results. In addition, with a more complicated  
406    semiempirical plume shape expression, one could have more control over plume shape and might be able  
407    to get an initial condition that yields a more accurate ash transport forecast. However, more complicated  
408    and adaptable plume shape expressions imply a higher dimensional parameter space, which requires more  
409    effort in calibration, even though the degrees of freedom to adjust plume shape are still limited. Creating  
410    initial conditions based on 3D plume simulations avoids such parameter calibration.

### 411    3.3 Horizontal Ash Distribution

412    The differences between the semiempirical plume particle distribution and actual (or simulated by the  
413    3D plume model) are not only in the vertical direction. The importance of the horizontal distance of each  
414    initial ash particle from a line extending upward from the volcano is investigated in this section. Puff  
415    uses a uniformly distributed random process to determine ash particle locations in a circle centered on the  
416    volcano site as described in section 2.2. For the output of Plume-SPH, an effective (maximum) radius is  
417    determined according to a given threshold of ash concentration, following Cerminara et al. (2016b). A time  
418    averaged, spatial integration of the dynamic 3D flow field is conducted to remove significant fluctuations  
419    in time and space. Fig. 9 compares the radius of the initial ash clouds created by 3D plume simulations

420 with that assumed in the semiempirical plume shape expression adopted in Puff. It is impossible for the  
421 simple, assumed plume shapes to capture the complex and more realistic shapes developed by Plume-SPH.  
422 Additional parameterization may generate more reasonable shapes, but these would continue to be *ad*  
423 *hoc*, none would likely have the potential fidelity of the 3D simulation to reality, and adding a temporally  
424 changing distribution would be difficult.

425 Comparison between cross-sectional views of the initial ash clouds is shown in Fig. 10. The cross-  
426 sectional view of horizontal particle distribution using the semiempirical method (last figure in Fig. 10)  
427 is similar to a cross-sectional view of a simulated 3D plume, in a general sense. However, for simulated  
428 3D plumes, the ash particle distribution in cross section varies with height, which factor would become  
429 increasingly important with increasing wind speed, were wind speed to be included in the estimate of initial  
430 plume shape. It is difficult for the semiempirical expressions to accommodate such a complex distribution.

431 Despite the obvious difficulty of correctly estimating ash distribution near the vent, or for short propagation  
432 times, assigning different values for the horizontal spread has a negligible effect on VATD simulation  
433 results at large time. We investigated horizontal spread values between 50 km and 1600 km to create initial  
434 ash clouds; all of them generated similar results at large propagation times ( $> 1$  day). Figure 11 shows  
435 two different simulation results based on initial ash clouds with horizontal spread equal to 50 km and 600  
436 km, respectively. No visible differences are apparent between them. The FMS values, 0.073 and 0.074,  
437 respectively, are also very close. This implies that horizontal distribution has a less significant influence on  
438 VATD simulation results than does vertical distribution for long distance or large time. Perhaps the most  
439 important ramification of this result is that it means the time at which the “handshake” is made between  
440 Plume-SPH and the VATD does not affect results significantly for relatively large distances and times.

## 4 DISCUSSION

### 4.1 Sensitivity of Other Inputs Parameters

442 Besides the initial ash cloud, other parameters for Puff simulations are: horizontal diffusivity, vertical  
443 diffusivity, mean grain size, grain size standard deviation and total number of tracers. We present in this  
444 subsection informal sensitivity studies on these parameters. We also investigate the influence of eruption  
445 duration. The sensitivity analyses will serve as the basis for identifying possible sources of disparities  
446 between simulation and observation.

447 Fero et al. (2008) simulated the volcanic ash transportation of Pinatubo eruption in 1991, he carried out  
448 systematic sensitivity analysis with respect to input parameters of Puff and found that all other parameters  
449 except for the plume height have negligible effect on long term ash transportation of Pinatubo. Inspired by  
450 Fero et al. (2008), we carried out similar informal sensitivity analysis with much fewer sample points in  
451 the parameter space and got similar results. Among the parameters explored, the eruption duration and  
452 beginning time show the most obvious influence on simulated ash distribution, although the effect is still  
453 small. To show the differences in an intuitive way, (a) - (c) in Fig. 12 shows simulated ash distribution  
454 corresponding to 4.9 hours duration, 9 hours duration and 11 hours duration, respectively. After 72 hours,  
455 relative to the simulation starting time, these three cases generate very similar results with tiny visible  
456 differences. Daniele et al. (2009) did sensitivity analysis with respect to the input parameters of Puff on  
457 different volcanoes and found that for eruptive eruptions, the most dominant factors are the wind field and  
458 plume height, while all other input parameters are relatively less important. The significance of the wind  
459 field has been confirmed by other researchers (Stefanescu et al., 2014, e.g) as well.

460 We conducted several simulations with eruption duration varying in the range of [5, 11] hours with  
461 slightly different starting time of climactic phase. Table 3 lists all these simulations. However, only slight

462 visible differences are observed among the simulated ash transport outputs. We can see that the eruption  
463 duration has negligible effects on long-term ash transport.

464 The new methodology for generating initial ash clouds introduces a new parameter: elevation threshold,  
465 which was specified based on averaged vertical velocity and horizontal velocity. We carry out a separate,  
466 informal sensitivity analysis on this parameter by varying the elevation threshold from 1.5 km (the height of  
467 the vent) to 25 m. The simulated ash distributions show obvious differences, especially when the elevation  
468 threshold is either very high or very low. However, varying the elevation threshold in the range of [12, 18]  
469 km generates relatively small differences in ash transport simulation results. Figure 12 (d) and (e) compare  
470 the simulated ash distributions corresponding to elevation thresholds of 1.5 km and 15 km. Compared with  
471 the ash distribution for a threshold of 15 km, an extra long tail appears when using an elevation threshold  
472 of 1.5 km. The maximum height of the tail is around 10 km. Adopting lower elevation thresholds adds  
473 more tracer particles at lower elevation. As the winds at different elevations are different, the tracers at  
474 lower elevations propagate in different directions. The HYSPLIT forward trajectory tracking indicates  
475 that the wind between elevations of 10 km and 15 km blew from north-east to south-west, while winds of  
476 higher elevation blew from east to west (see Fig. 6).

## 477 4.2 Other Sources of Disparities

478 The full range of research issues raised by numerical forecasting of volcanic clouds is diverse. We focused  
479 on the effect of initial conditions in this paper. During the plume modeling, secondary factors, such as  
480 microphysical processes, even though they play lesser roles, likely need to be included to improve accuracy  
481 for a particular eruption. Wind fields are not considered in the current version of Plume-SPH, but for weak  
482 plumes, wind plays such an important role that it has to be considered in the plume model. In addition,  
483 eruption conditions are subject to change with time, even during the climactic phase of an eruption. For  
484 example, ash just west of Pinatubo observed in satellite images does not show up in “Plume-SPH + Puff”  
485 simulation results. This disparity is likely due to the fact that Pinatubo continued erupting after the climactic  
486 phase, while we only simulate the climactic phase. In the future, time-dependent initial conditions for  
487 VATDs can be created from 3D plume simulations based on time-dependent eruption conditions. Worth to  
488 mention that the eruption conditions at the vent are usually inferred from observable information based on  
489 1D plume models. Using a 3D plume model won’t reduce uncertainties from the eruption conditions.

490 Assumption made in each VATD model is another source of errors. For example, a recent study by Osman  
491 et al. (2020) demonstrated the great impact of GSD on modelled ash mass loadings using NAME(Jones  
492 et al., 2007) to simulate historical eruptions of various VEIs. Other researchers (Beckett et al., 2015; Scollo  
493 et al., 2008) have proven the significance of GSD using other VATD models. Their conclusion, however, is  
494 different from our informal sensitivity study and other more comprehensive sensitivity studies using Puff.  
495 This might be because of different assumptions made in different VATD models. These assumptions may  
496 lead to underestimation or overestimation of certain factors, such as GSD.

497 One implicit assumption in the current method is that ash transportation is dominated by wind advection  
498 (the passive dispersion approximation). However, during the growth of volcanic umbrella, the dominant  
499 factors are various in different regimes (Pouget et al., 2016a) depending on characteristics of a particular  
500 eruption. Webster et al. (2020) suggested that the lateral spread by the intrusive gravity current dominates  
501 the transport of the ash cloud in this stage. A few studies by Larry Mastin (Mastin et al., 2014; Mastin  
502 and Van Eaton, 2020) also showed that neglecting the umbrella cloud formation for larger eruptions led to  
503 significantly different footprints for the resulting VATD fallout maps. Their studies imply that including  
504 mapped velocities of the plume as a perturbation on the winds can better capture the radial spreading  
505 of umbrella. In the current method, the 3D plume model generated initial ash cloud has a radius around

506 25 km. For the Pinatubo 1991 eruption, the passive dispersion approximation can be reasonably applied  
507 when radius is greater than 450 km, and can be fully valid only when the radius is greater than 1800 km  
508 (Costa et al., 2013). It is computationally too expensive for the Plume-SPH model to simulate a volcanic  
509 umbrella. An umbrella model, with much coarse resolution, in between plume model and VATD model  
510 would presumably better model the whole ash transportation process.

511 Besides the errors from assumptions of the model, errors are also introduced from the reanalysis wind  
512 field data and the satellite observations, which are retrievals other than the “truth”. In addition, metrics  
513 based on footprint can not account for the disparities at different height and ash concentration. Comparing  
514 the simulation and observation purely based on footprint based metric sometimes is biased.

### 515 4.3 Summary

516 This paper presents, for the first time, VATD simulations using initial source conditions created by a 3D  
517 plume model. Traditional VATD simulations use initial conditions created according to a semiempirical  
518 plume shape expression. A case study of the 1991 Pinatubo eruption demonstrates that a 3D plume model  
519 can create more realistic initial ash cloud and ash parcel positions, and therefore improve the accuracy of  
520 ash transport forecasts. Informal sensitivity analyses suggest that initial conditions, as expressed in the  
521 disposition of initial ash parcel positions in the vertical, have a more significant effect on a volcanic ash  
522 transport forecast than most other parameters. Comparison of initial ash parcel distributions among the  
523 3D plume model, semiempirical expressions, and observations suggests that a major subpopulation of ash  
524 parcels should be placed at a much lower elevation than plume height to obtain a better VATD forecast.  
525 Comparing the effects of the plume height, vertical spread and horizontal spread shows that ash particle  
526 distribution in the vertical direction has the strongest effect on VATD simulation.

527 To summarize, we have presented a novel method for creating *a priori* initial source conditions for  
528 VATD simulations. We have shown that it might be possible to obtain initial positions of ash parcels  
529 with deterministic forward modeling of the volcanic plume, potentially obviating or lessening the need to  
530 attempt to somehow observe initial positions, or *a posteriori* create a history of release heights via inversion  
531 (Stohl et al., 2011). Although the method now suffers from the high computational cost associated with  
532 3D forward modeling, there is the possibility that in future it might not only help overcome shortcomings  
533 of existing methods used to generate *a priori* input parameters, but also overcome the need to carry out  
534 thousands of runs associated with inverse modeling. In addition, computational cost will continue to  
535 diminish as computing speed increases. As they are forward numerical models based on first principles,  
536 3D plume models need little if any parameterization, and user intervention should not be required to  
537 improve forecast power; no assumption about the initial position of ash parcels is needed. Generation of the  
538 initial cloud of ash parcels directly by 3D simulation is potentially adaptable to a variety of volcanic and  
539 atmospheric scenarios. In contrast, semiempirical expressions used to determine initial conditions require  
540 several parameters to control ash particle distribution along a vertical line source or some simplified shape  
541 of the initial ash cloud, making it difficult in some cases to generate initial conditions that closely resemble  
542 a complex reality.

## CONFLICT OF INTEREST STATEMENT

543 The authors declare that the research was conducted in the absence of any commercial or financial  
544 relationships that could be construed as a potential conflict of interest.

## AUTHOR CONTRIBUTIONS

545 The idea of using a 3D plume model to start a VATD simulation originated from a conservation between  
546 AP and MB. ZC carried out the Plume-SPH simulations, Puff simulations, initial results analysis, and  
547 prepared the first draft. All authors worked together for further revisions. MB carried out the HYSPLIT  
548 simulation. QY post-processed the Puff simulation results, overlapped the simulation results with satellite  
549 observation, and calculated the FMS values. All authors contributed equally to the manuscript writing. AP  
550 and MB obtained funding to financially support the work.

## FUNDING

551 This work was supported by National Science Foundation awards 1521855, 1621853, and 1821311,  
552 1821338 and 2004302 and by the National Research Foundation Singapore and the Singapore Ministry  
553 of Education under the Research Centres of Excellence initiative (project number: NRF2018NRF-  
554 NSFC003ES-010).

## ACKNOWLEDGMENTS

555 We are grateful to the two anonymous reviewers of the paper for their constructive comments and suggesti-  
556 ons that improved the paper. Support for the Twentieth Century Reanalysis Project dataset is provided by  
557 the U.S. Department of Energy, Office of Science Innovative and Novel Computational Impact on Theory  
558 and Experiment (DOE INCITE) program, and Office of Biological and Environmental Research (BER),  
559 and by the National Oceanic and Atmospheric Administration Climate Program Office.

## REFERENCES

- 560 Avdyushin, S., Tulinov, G., Ivanov, M., Kuzmenko, B., Mezhuev, I., Nardi, B., et al. (1993). 1. spatial and  
561 temporal evolution of the optical thickness of the pinatubo aerosol cloud in the northern hemisphere  
562 from a network of ship-borne and stationary lidars. *Geophysical research letters* 20, 1963–1966
- 563 Beckett, F., Witham, C., Hort, M., Stevenson, J., Bonadonna, C., and Millington, S. (2015). Sensitivity of  
564 dispersion model forecasts of volcanic ash clouds to the physical characteristics of the particles. *Journal*  
565 *of Geophysical Research: Atmospheres* 120, 11–636
- 566 Bonadonna, C., Connor, C. B., Houghton, B., Connor, L., Byrne, M., Laing, A., et al. (2005). Probabilistic  
567 modeling of tephra dispersal: Hazard assessment of a multiphase rhyolitic eruption at tarawera, new  
568 zealand. *Journal of Geophysical Research: Solid Earth* 110
- 569 Bonadonna, C. and Houghton, B. (2005). Total grain-size distribution and volume of tephra-fall deposits.  
570 *Bulletin of Volcanology* 67, 441–456
- 571 Bursik, M. (2001). Effect of wind on the rise height of volcanic plumes. *Geophys. Res. Lett* 28, 3621–3624
- 572 Bursik, M., Jones, M., Carn, S., Dean, K., Patra, A., Pavolonis, M., et al. (2012). Estimation and  
573 propagation of volcanic source parameter uncertainty in an ash transport and dispersal model: application  
574 to the eyjafjallajokull plume of 14–16 april 2010. *Bulletin of volcanology* 74, 2321–2338
- 575 Bursik, M., Kobs, S., Burns, A., Braitseva, O., Bazanova, L., Melekestsev, I., et al. (2009). Volcanic  
576 plumes and wind: Jetstream interaction examples and implications for air traffic. *Journal of Volcanology*  
577 *and Geothermal Research* 186, 60–67
- 578 Cao, Z., Patra, A., Bursik, M., Pitman, E. B., and Jones, M. (2018). Plume-sph 1.0: a three-dimensional,  
579 dusty-gas volcanic plume model based on smoothed particle hydrodynamics. *Geoscientific Model*  
580 *Development* 11, 2691–2715
- 581 Cao, Z., Patra, A., and Jones, M. (2017). Data management and volcano plume simulation with parallel  
582 sph method and dynamic halo domains. *Procedia Computer Science* 108, 786–795

- 583 Cerminara, M., Esposti Ongaro, T., and Berselli, L. (2016a). Ashee-1.0: a compressible, equilibrium-  
584 eularian model for volcanic ash plumes. *Geoscientific Model Development* 9, 697–730
- 585 Cerminara, M., Esposti Ongaro, T., and Neri, A. (2016b). Large eddy simulation of gas–particle kinematic  
586 decoupling and turbulent entrainment in volcanic plumes. *Journal of Volcanology and Geothermal  
587 Research*
- 588 Constantinescu, R., Hopulele-Gligor, A., Connor, C. B., Bonadonna, C., Connor, L. J., Lindsay, J. M.,  
589 et al. (2021). The radius of the umbrella cloud helps characterize large explosive volcanic eruptions.  
590 *Communications Earth & Environment* 2, 1–8
- 591 Costa, A., Folch, A., and Macedonio, G. (2013). Density-driven transport in the umbrella region of volcanic  
592 clouds: Implications for tephra dispersion models. *Geophysical Research Letters* 40, 4823–4827
- 593 Costa, A., Suzuki, Y., Cerminara, M., Devenish, B., Esposti Ongaro, T., Herzog, M., et al. (2016). Results  
594 of the eruptive column model inter-comparison study. *Journal of Volcanology and Geothermal Research*
- 595 D'amours, R. (1998). Modeling the etex plume dispersion with the canadian emergency response model.  
596 *Atmospheric Environment* 32, 4335–4341
- 597 Daniele, P., Lirer, L., Petrosino, P., Spinelli, N., and Peterson, R. (2009). Applications of the puff model to  
598 forecasts of volcanic clouds dispersal from etna and vesuvio. *Computers & Geosciences* 35, 1035–1049
- 599 DeFoor, T. E., Robinson, E., and Ryan, S. (1992). Early lidar observations of the june 1991 pinatubo  
600 eruption plume at mauna loa observatory, hawaii. *Geophysical research letters* 19, 187–190
- 601 de'Michieli Vitturi, M., Neri, A., and Barsotti, S. (2015). Plume-mom 1.0: A new integral model of  
602 volcanic plumes based on the method of moments. *Geoscientific Model Development* 8, 2447–2463
- 603 Deshler, T., Hofmann, D., Johnson, B., and Rozier, W. (1992). Balloonborne measurements of the pinatubo  
604 aerosol size distribution and volatility at laramie, wyoming during the summer of 1991. *Geophysical  
605 research letters* 19, 199–202
- 606 Draxler, R. R. and Hess, G. (1998). An overview of the hysplit\_4 modelling system for trajectories.  
607 *Australian meteorological magazine* 47, 295–308
- 608 Fero, J., Carey, S. N., and Merrill, J. T. (2008). Simulation of the 1980 eruption of mount st. helens using  
609 the ash-tracking model puff. *Journal of Volcanology and Geothermal Research* 175, 355–366
- 610 Fero, J., Carey, S. N., and Merrill, J. T. (2009). Simulating the dispersal of tephra from the 1991  
611 pinatubo eruption: implications for the formation of widespread ash layers. *Journal of Volcanology and  
612 Geothermal Research* 186, 120–131
- 613 Folch, A., Costa, A., and Macedonio, G. (2009). Fall3d: A computational model for transport and  
614 deposition of volcanic ash. *Computers & Geosciences* 35, 1334–1342
- 615 Folch, A., Costa, A., and Macedonio, G. (2016). Fplume-1.0: An integral volcanic plume model accounting  
616 for ash aggregation. *Geoscientific Model Development* 9, 431
- 617 Gingold, R. A. and Monaghan, J. J. (1977). Smoothed particle hydrodynamics: theory and application to  
618 non-spherical stars. *Monthly notices of the royal astronomical society* 181, 375–389
- 619 Guo, S., Bluth, G. J., Rose, W. I., Watson, I. M., and Prata, A. (2004a). Re-evaluation of so2 release  
620 of the 15 june 1991 pinatubo eruption using ultraviolet and infrared satellite sensors. *Geochemistry,  
621 Geophysics, Geosystems* 5
- 622 Guo, S., Rose, W. I., Bluth, G. J., and Watson, I. M. (2004b). Particles in the great pinatubo volcanic cloud  
623 of june 1991: The role of ice. *Geochemistry, Geophysics, Geosystems* 5
- 624 Heffter, J. L. and Stunder, B. J. (1993). Volcanic ash forecast transport and dispersion (vaftad) model.  
625 *Weather and forecasting* 8, 533–541
- 626 Holasek, R., Self, S., and Woods, A. (1996a). Satellite observations and interpretation of the 1991 mount  
627 pinatubo eruption plumes. *Journal of Geophysical Research: Solid Earth* 101, 27635–27655

- 628 Holasek, R. E., Woods, A. W., and Self, S. (1996b). Experiments on gas-ash separation processes in  
629 volcanic umbrella plumes. *Journal of volcanology and geothermal research* 70, 169–181
- 630 Jäger, H. (1992). The pinatubo eruption cloud observed by lidar at garmisch-partenkirchen. *Geophysical*  
631 *research letters* 19, 191–194
- 632 Jones, A., Thomson, D., Hort, M., and Devenish, B. (2007). The uk met office's next-generation  
633 atmospheric dispersion model, name iii. In *Air pollution modeling and its application XVII* (Springer).  
634 580–589
- 635 Mastin, L. G. (2007). A user-friendly one-dimensional model for wet volcanic plumes. *Geochemistry,*  
636 *Geophysics, Geosystems* 8
- 637 Mastin, L. G. and Van Eaton, A. R. (2020). Comparing simulations of umbrella-cloud growth and ash  
638 transport with observations from pinatubo, kelud, and calbuco volcanoes. *Atmosphere* 11, 1038
- 639 Mastin, L. G., Van Eaton, A. R., and Lowenstern, J. B. (2014). Modeling ash fall distribution from a  
640 yellowstone supereruption. *Geochemistry, Geophysics, Geosystems* 15, 3459–3475
- 641 Neri, A., Esposti Ongaro, T., Macedonio, G., and Gidaspow, D. (2003). Multiparticle simulation of  
642 collapsing volcanic columns and pyroclastic flow. *Journal of Geophysical Research: Solid Earth*  
643 (1978–2012) 108
- 644 Oberhuber, J. M., Herzog, M., Graf, H.-F., and Schwanke, K. (1998). Volcanic plume simulation on large  
645 scales. *Journal of Volcanology and Geothermal Research* 87, 29–53
- 646 Osman, S., Beckett, F., Rust, A., and Snee, E. (2020). Sensitivity of volcanic ash dispersion modelling to  
647 input grain size distribution based on hydromagmatic and magmatic deposits. *Atmosphere* 11, 567
- 648 Paladio-Melosantos, M. L. O., Solidum, R. U., Scott, W. E., Quiambao, R. B., Umbal, J. V., Rodolfo, K. S.,  
649 et al. (1996). Tephra falls of the 1991 eruptions of mount pinatubo. *Fire and mud* 12000, 12030
- 650 Pfeiffer, T., Costa, A., and Macedonio, G. (2005). A model for the numerical simulation of tephra fall  
651 deposits. *Journal of Volcanology and Geothermal Research* 140, 273–294
- 652 Pouget, S., Bursik, M., Johnson, C. G., Hogg, A. J., Phillips, J. C., and Sparks, R. S. J. (2016a).  
653 Interpretation of umbrella cloud growth and morphology: implications for flow regimes of short-lived  
654 and long-lived eruptions. *Bulletin of Volcanology* 78, 1–19
- 655 Pouget, S., Bursik, M., Singla, P., and Singh, T. (2016b). Sensitivity analysis of a one-dimensional model  
656 of a volcanic plume with particle fallout and collapse behavior. *Journal of Volcanology and Geothermal*  
657 *Research*
- 658 Rolph, G., Stein, A., and Stunder, B. (2017). Real-time environmental applications and display system:  
659 Ready. *Environmental Modelling & Software* 95, 210–228
- 660 Schwaiger, H. F., Denlinger, R. P., and Mastin, L. G. (2012). Ash3d: A finite-volume, conservative  
661 numerical model for ash transport and tephra deposition. *Journal of Geophysical Research: Solid Earth*  
662 117
- 663 Scollo, S., Folch, A., and Costa, A. (2008). A parametric and comparative study of different tephra fallout  
664 models. *Journal of Volcanology and Geothermal Research* 176, 199–211
- 665 Scott, W. E., Hoblitt, R. P., Torres, R. C., Self, S., Martinez, M. M. L., and Nillos, T. (1996). Pyroclastic  
666 flows of the june 15, 1991, climactic eruption of mount pinatubo. *Fire and Mud: eruptions and lahars of*  
667 *Mount Pinatubo, Philippines*, 545–570
- 668 Searcy, C., Dean, K., and Stringer, W. (1998). Puff: A volcanic ash tracking and prediction model. *Journal*  
669 *of Volcanology and Geothermal Research* 80, 1–16
- 670 Self, S., Zhao, J.-X., Holasek, R. E., Torres, R. C., and King, A. J. (1996). The atmospheric impact of the  
671 1991 mount pinatubo eruption

- 672 Stefanescu, E., Patra, A. K., Bursik, M., Jones, M., Madankan, R., Pitman, E. B., et al. (2014). Fast  
673 construction of surrogates for uq central to dddas—application to volcanic ash transport. *Procedia  
674 Computer Science* 29, 1227–1235
- 675 Stein, A., Draxler, R., Rolph, G., Stunder, B., Cohen, M., and Ngan, F. (2015). Noaa's hysplit atmospheric  
676 transport and dispersion modeling system. *Bulletin of the American Meteorological Society* 96, 2059–  
677 2077
- 678 Stohl, A., Prata, A., Eckhardt, S., Clarisse, L., Durant, A., Henne, S., et al. (2011). Determination of  
679 time-and height-resolved volcanic ash emissions and their use for quantitative ash dispersion modeling:  
680 the 2010 eyjafjallajökull eruption. *Atmospheric Chemistry and Physics* 11, 4333–4351
- 681 Suzuki, T. et al. (1983). A theoretical model for dispersion of tephra. *Arc volcanism: physics and tectonics*  
682 95, 113
- 683 Suzuki, Y. and Koyaguchi, T. (2009). A three-dimensional numerical simulation of spreading umbrella  
684 clouds. *Journal of Geophysical Research: Solid Earth (1978–2012)* 114
- 685 Suzuki, Y. J., Koyaguchi, T., Ogawa, M., and Hachisu, I. (2005). A numerical study of turbulent mixing  
686 in eruption clouds using a three-dimensional fluid dynamics model. *Journal of Geophysical Research: Solid Earth* 110
- 687 Tanaka, H. (1991). Development of a prediction scheme for the volcanic ash fall from redoubt volcano. In  
688 *First Int'l. Symp. on Volcanic Ash and Aviation Safety*. vol. 58
- 689 Tupper, A., Itikarai, I., Richards, M., Prata, F., Carn, S., and Rosenfeld, D. (2007). Facing the challenges of  
690 the international airways volcano watch: the 2004/05 eruptions of manam, papua new guinea. *Weather and Forecasting* 22, 175–191
- 691 Walko, R., Tremback, C., and Bell, M. (1995). Hypact: The hybrid particle and concentration transport  
692 model. *User's guide*
- 693 Webster, H. N., Devenish, B. J., Mastin, L. G., Thomson, D. J., and Van Eaton, A. R. (2020). Operational  
694 modelling of umbrella cloud growth in a lagrangian volcanic ash transport and dispersion model.  
695 *Atmosphere* 11, 200
- 696 Witham, C., Hort, M., Potts, R., Servranckx, R., Husson, P., and Bonnardot, F. (2007). Comparison of  
697 vaac atmospheric dispersion models using the 1 november 2004 grimsvötn eruption. *Meteorological  
698 Applications* 14, 27–38
- 699 Woods, A. (1988). The fluid dynamics and thermodynamics of eruption columns. *Bulletin of Volcanology*  
700 50, 169–193
- 701 Zidikheri, M. J., Lucas, C., and Potts, R. J. (2017). Estimation of optimal dispersion model source  
702 parameters using satellite detections of volcanic ash. *Journal of Geophysical Research: Atmospheres*  
703 122, 8207–8232

## FIGURE CAPTIONS

706 T

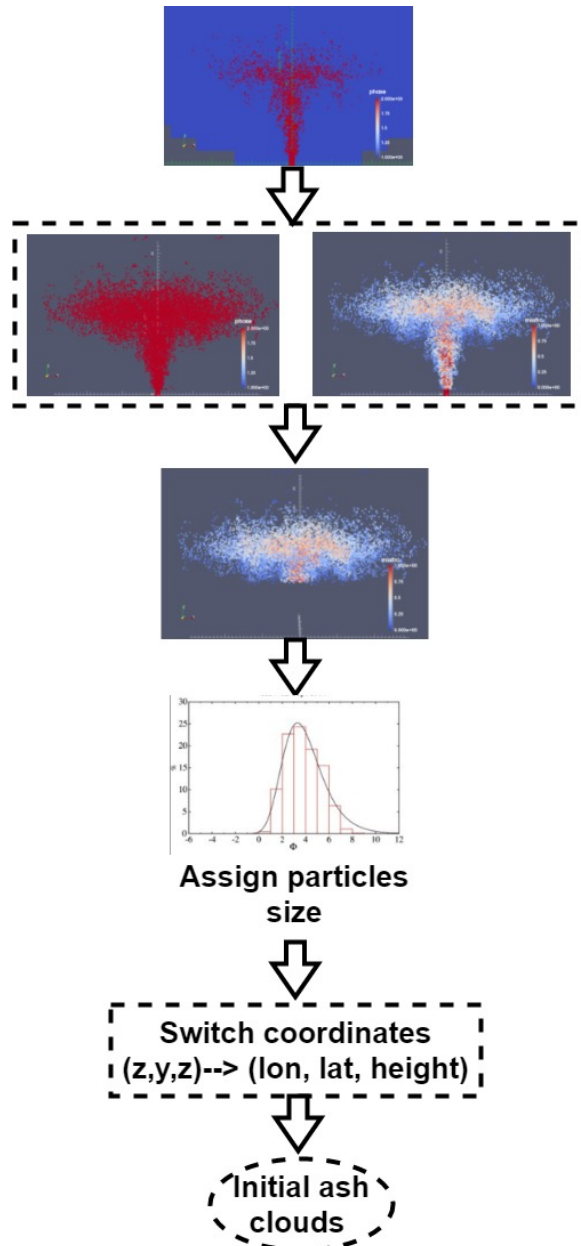


**Figure 1.** Steps to create initial condition for Puff based on raw output of Plume-SPH (Cao et al., 2018). First row: raw output of Plume-SPH. Blue particles are phase 1 (ambient air), red particles are phase 2 (erupted material). Second row: plume after removing SPH particles of phase 1. Picture at right is colored according to the mass fraction of erupted material. Third row: volcanic plume above the “corner” region after cutting off the lower portion. Fourth row: assign sizes to particles converting numerical discretization points into tracers. Fifth row: switch coordinates in local coordinate system into (*longitude, latitude, height*)

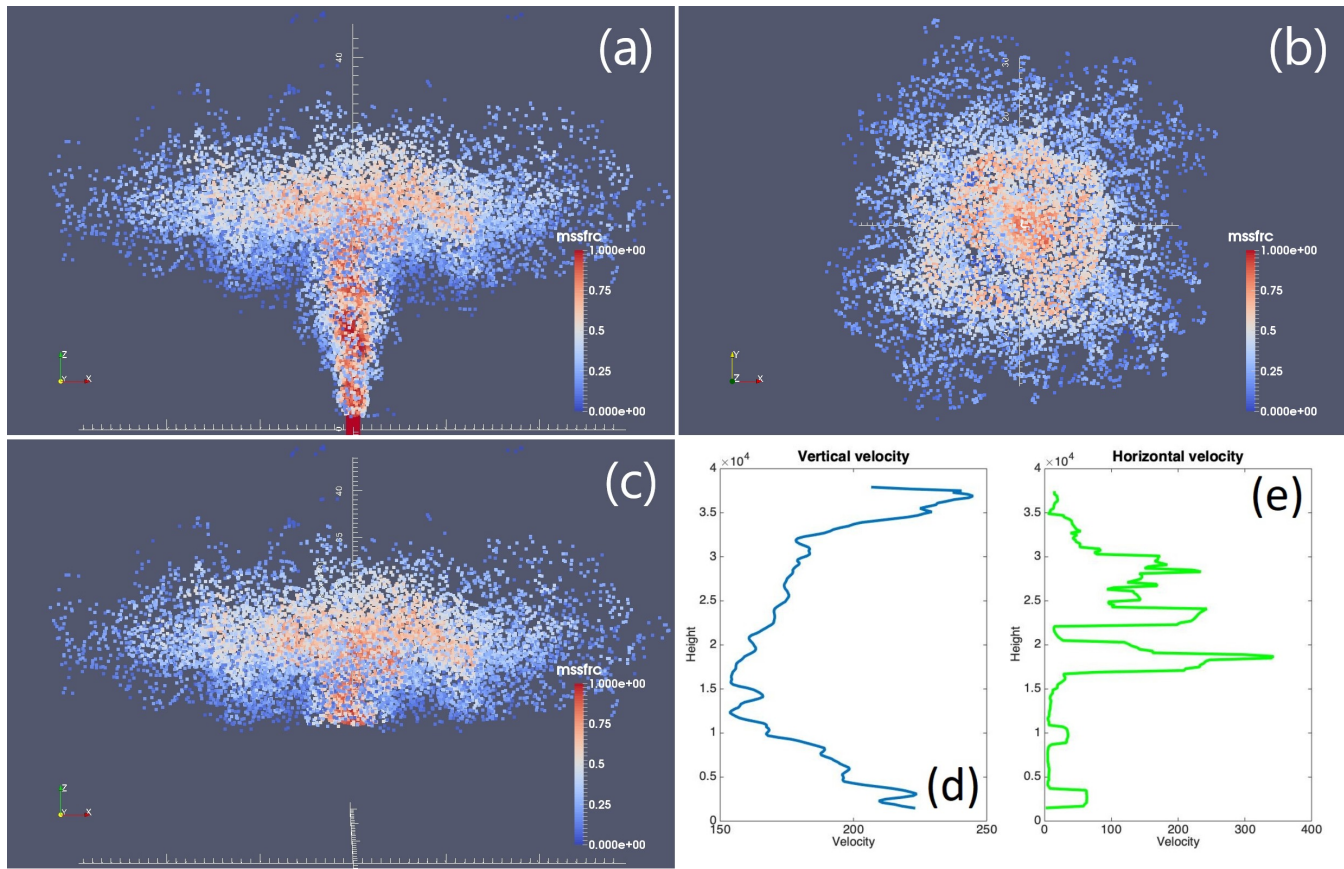


**Figure 2.** Volcano plume from 3D plume model. All particles in the pictures are of phase 2 (particle of phase 1 has been removed) at 600s after eruption, at which time, the plume has already reached the plume height and started spreading radially. (a) is front view of the whole plume. (b) is top view of the plume. (c) is front view of the initial ash cloud, which is essentially a portion of the whole plume whose elevation is higher than a given threshold (in this picture is 15 km). Particles are colored according to mass fraction of erupted material. Red represents high mass fraction while blue represents low mass fraction. (d) is averaged vertical velocity of the plume. At elevations below 15 km, the average vertical velocity decreases. At elevations higher 15 km, the averaged vertical velocity starts increasing. (e) is averaged horizontal velocity of the plume. The averaged horizontal velocity becomes obviously larger when elevation is higher than 15 km. So the reflection point is somewhere around 15 km.

**Table 1.** List of eruption condition and material properties for plume simulation

Parameters	Units	Plume
Vent Velocity	$\text{m} \cdot \text{s}^{-1}$	275
Vent Gas Mass Fraction		0.05
Vent Temperature	K	1053
Vent Height	m	1500
Mass Discharge Rate	$\text{kg} \cdot \text{s}^{-1}$	$1.5 \times 10^9$
Specific Heat of Gas at Constant Volume	$\text{J} \cdot \text{kg}^{-1} \cdot \text{K}^{-1}$	717
Specific Heat of Air at Constant Volume	$\text{J} \cdot \text{kg}^{-1} \cdot \text{K}^{-1}$	1340
Specific Heat of Solid	$\text{J} \cdot \text{kg}^{-1} \cdot \text{K}^{-1}$	1100
Specific Heat of Gas at Constant Pressure	$\text{J} \cdot \text{kg}^{-1} \cdot \text{K}^{-1}$	1000
Specific Heat of Air at Constant Pressure	$\text{J} \cdot \text{kg}^{-1} \cdot \text{K}^{-1}$	1810
Density of Air at Vent Height	$\text{kg} \cdot \text{m}^{-3}$	1.104
Pressure at Vent Height	Pa	84363.4

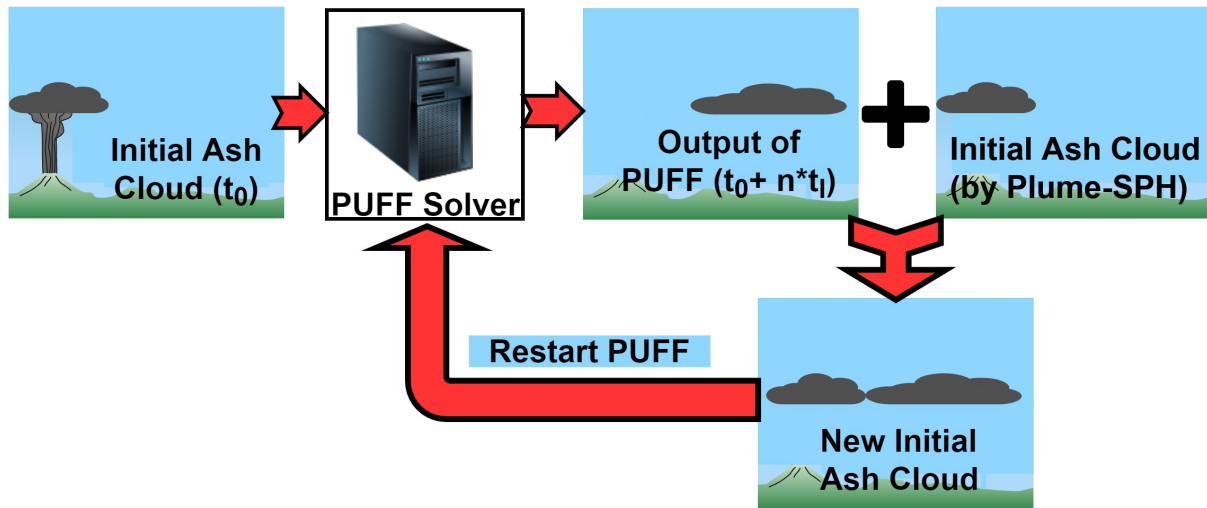


**Figure 3.** Mimic successive eruption with intermittent pulsed releasing of ash particles.  $t_I$  is the period of pulsing release.  $t_I$  equals the physical time of 3D plume simulation.

**Table 2.** Parameters used in VATD simulation of the climactic phase of Pinatubo eruption on June 15 1991. The first six parameters are used by semiempirical expression to create an initial ash cloud. When creating an initial condition based on the Plume-SPH model, these parameters are extracted from output of Plume-SPH model.

Parameters	Unit	Semiempirical	Plume-SPH
Plume Height ( $H_{max}$ )	km	40	-
Horizontal Spread ( $r_{max}$ )	km	103.808	-
Vertical Spread ( $H_{width}$ )	km	6.662	-
Plume Shape	-	Poisson	-
Total Ash Particles	-	1768500	1768500
Elevation Threshold	m	-	15000
Horizontal Diffusivity	$m^2/s$	10000	10000
Vertical Diffusivity	$m^2/s$	10	10
Grain Size Distribution	-	Gaussian	Gaussian
Mean of Grain Size (Radius)	mm	$3.5 \times 10^{-2}$	$3.5 \times 10^{-2}$
Standard Deviation of Grain Size	-	1.0	1.0
Start Time	UT	0441	0441
End time	UT	1341	1341
Simulation Duration	hour	72	72

**Table 3.** The starting and ending time (UT) for simulating the climactic phase of Pinatubo eruption on June 15 1991. Observed plume height (Holasek et al., 1996a) at different time are also listed in the table.

Eruption Duration	4.9 hours	9 hours	10 hours	11.1 hours
Start Time	0441	0441	0441	0334
Height at Start Time	37.5 km	37.5 km	37.5 km	24.5 km
End Time	0934	1341	1441	1441
Height at End Time	35 km	26.5 km	22.5	22.5 km

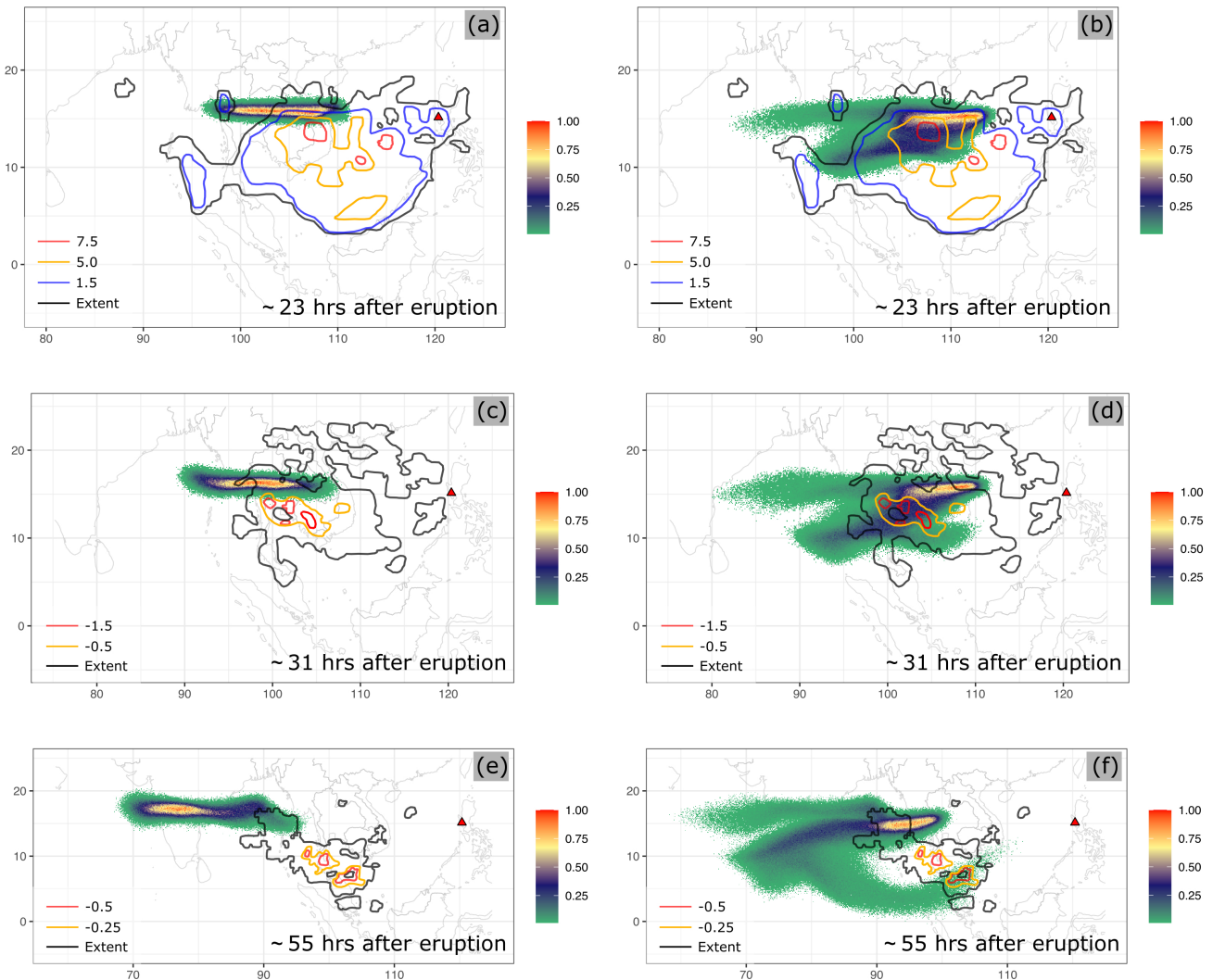


**Figure 4.** Comparison between “Semiempirical initial cloud + Puff” and “Plume-SPH + Puff”. Pictures to the left are: Puff simulation based on initial condition created according to semiempirical plume shape expression. Pictures to the right are Puff simulation based on initial condition generated by Plume-SPH. TOMS or AVHRR image of Pinatubo ash cloud are overlapped with the simulation results. Ash clouds at different hours after eruption are on different rows. From top to bottom, the images are corresponding to around 23 hours after eruption (UT 199106160341), 31 hours after eruption (UT 199106161141), 55 hours after eruption (UT 199106171141). The observation data on the first row are TOMS ash and ice map. The observation data on the second and third row are AVHRR BTD ash cloud map with atmospheric correction method applied (Guo et al., 2004b). The contours of simulation results are maximum concentration at given (*longitude, latitude*).

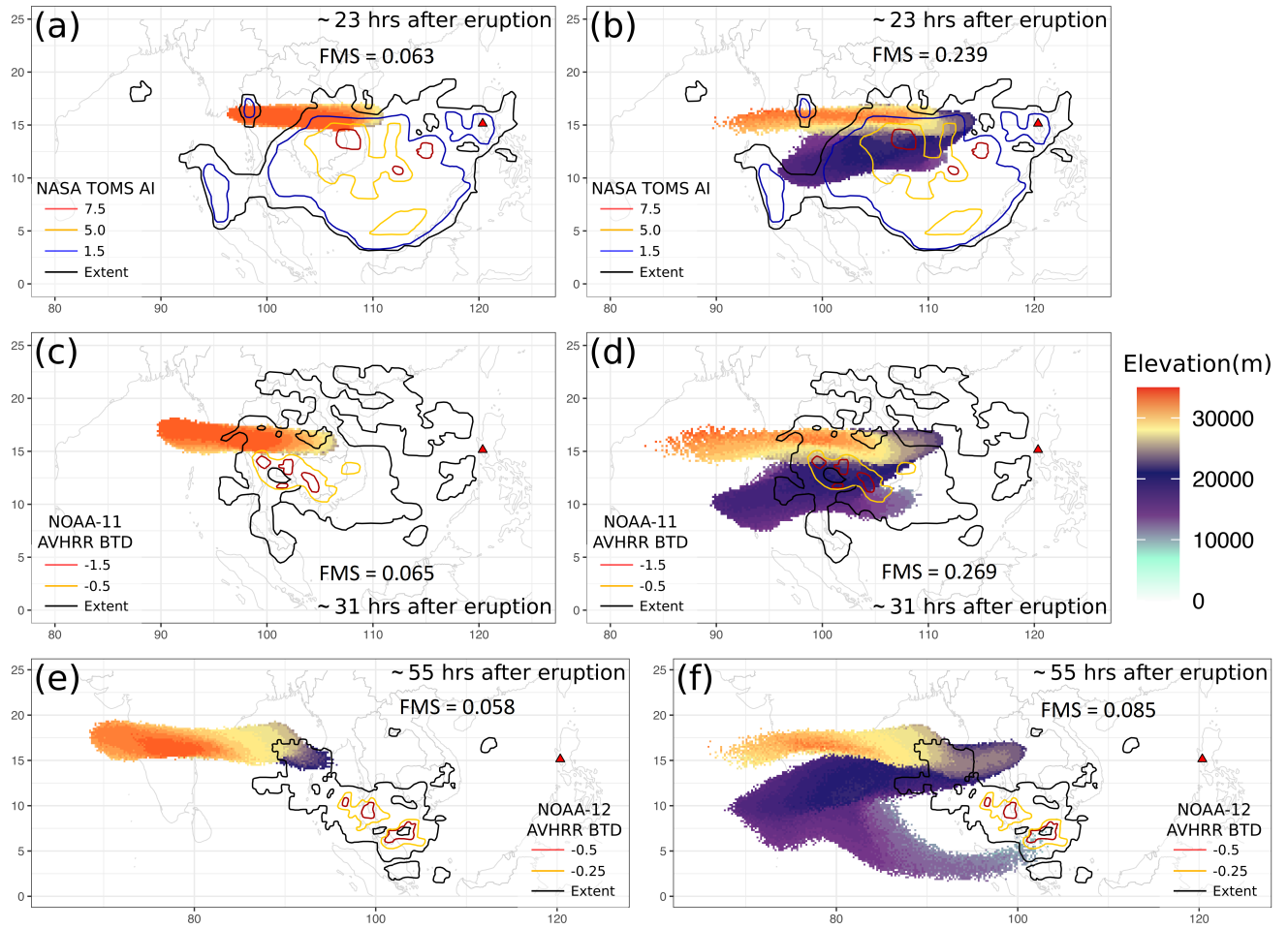


**Figure 5.** Comparison between “Semiempirical initial cloud + Puff” and “Plume-SPH + Puff”. Pictures to the left are: Puff simulation based on initial condition created according to semiempirical plume shape expression. Pictures to the right are Puff simulation based on initial condition generated by Plume-SPH. TOMS or AVHRR image of Pinatubo ash cloud are overlapped with the simulation results. Ash clouds at different hours after eruption are on different rows. From top to bottom, the images are corresponding to around 23 hours after eruption (UT 199106160341), 31 hours after eruption (UT 199106161141), 55 hours after eruption (UT 199106171141). The observation data on the first row are TOMS ash and ice map. The observation data on the second and third row are AVHRR BTD ash cloud map with atmospheric correction method applied (Guo et al., 2004b). The contours of simulation results are maximum height of ash cloud. The FMS value for each simulation is on each contour.

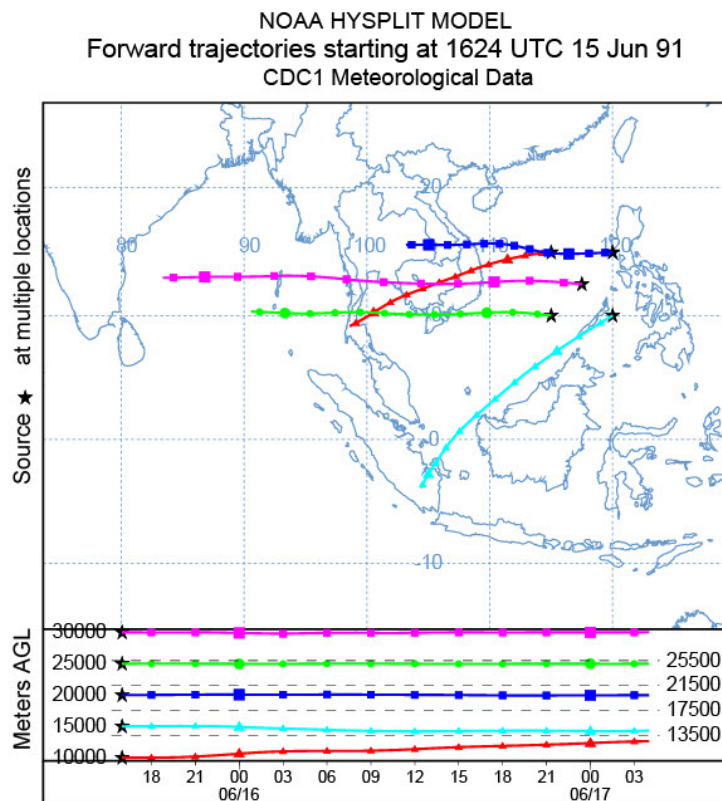


**Figure 6.** Trajectories of particles starting from different heights indicating the wind directions of different evaluations. The trajectories are chosen to start at points that were on the perimeter of the umbrella cloud in  $x$ ,  $y$  and  $z$ , and in its center, right before it became affected by the wind to give an idea of the maximum possible spread of the trajectories from that initial condition.

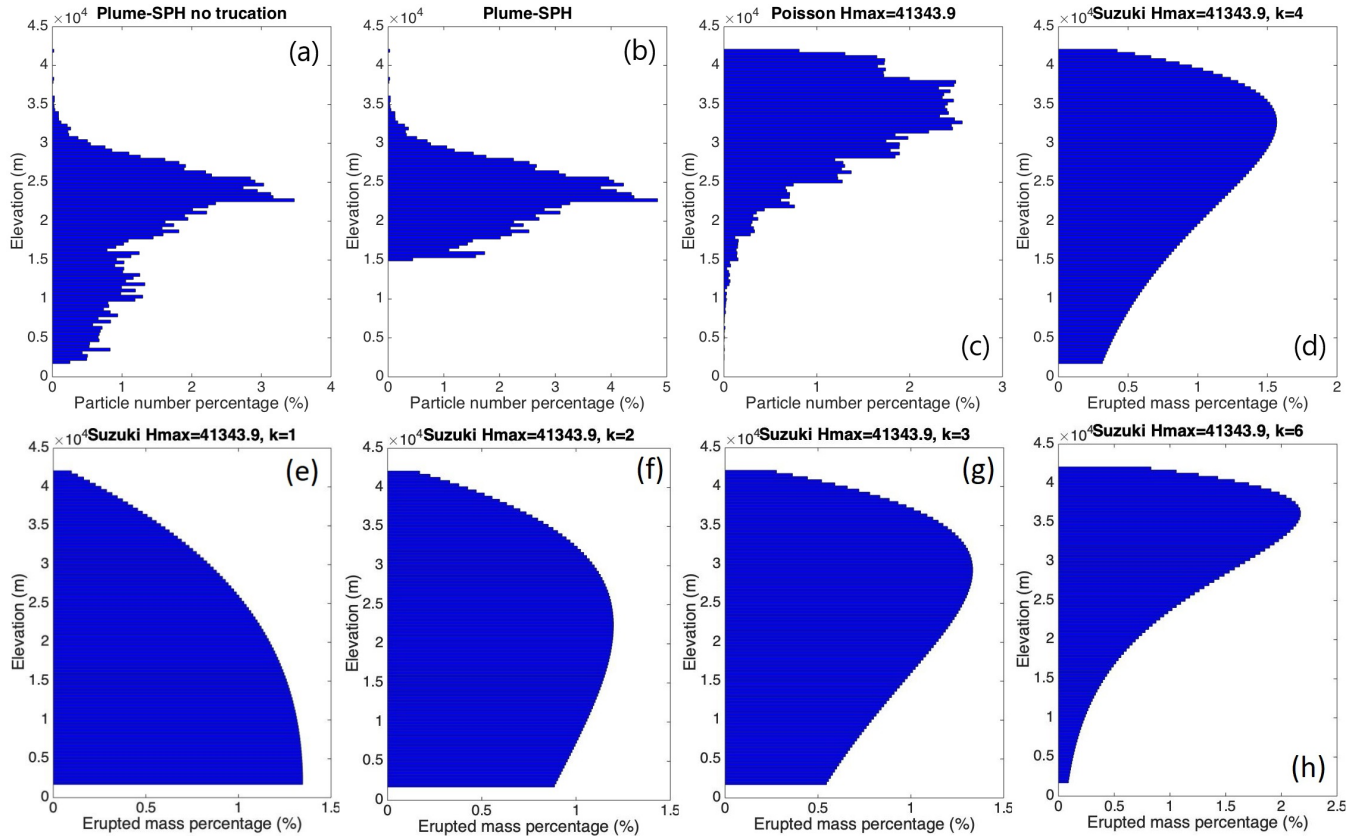


**Figure 7.** First row, comparison of particle distribution of initial ash cloud in vertical direction. (a) is corresponding to the initial ash cloud obtained from Plume-SPH output. (b) is (a) truncated by a elevation threshold of 15 km. (c) is for vertical ash distribution based on Poisson distribution (Eq. (13)) with  $H_{max}$  equals to 40 km. Another parameter,  $H_{width}$  is 6662 m. (d) is corresponding to Suzuki distribution (Eq. (14)) with  $H_{max}$  equals to 40 km and  $k$  equals to 4(Pfeiffer et al., 2005). The second row, Suzuki distribution with  $H_{max}$  equals to 40 km but different values for  $k$ . The  $x$  axis is the percentage of particle numbers for Plume-SPH and Poisson. For Suzuki the  $x$  axis is the mass percentage of erupted material.

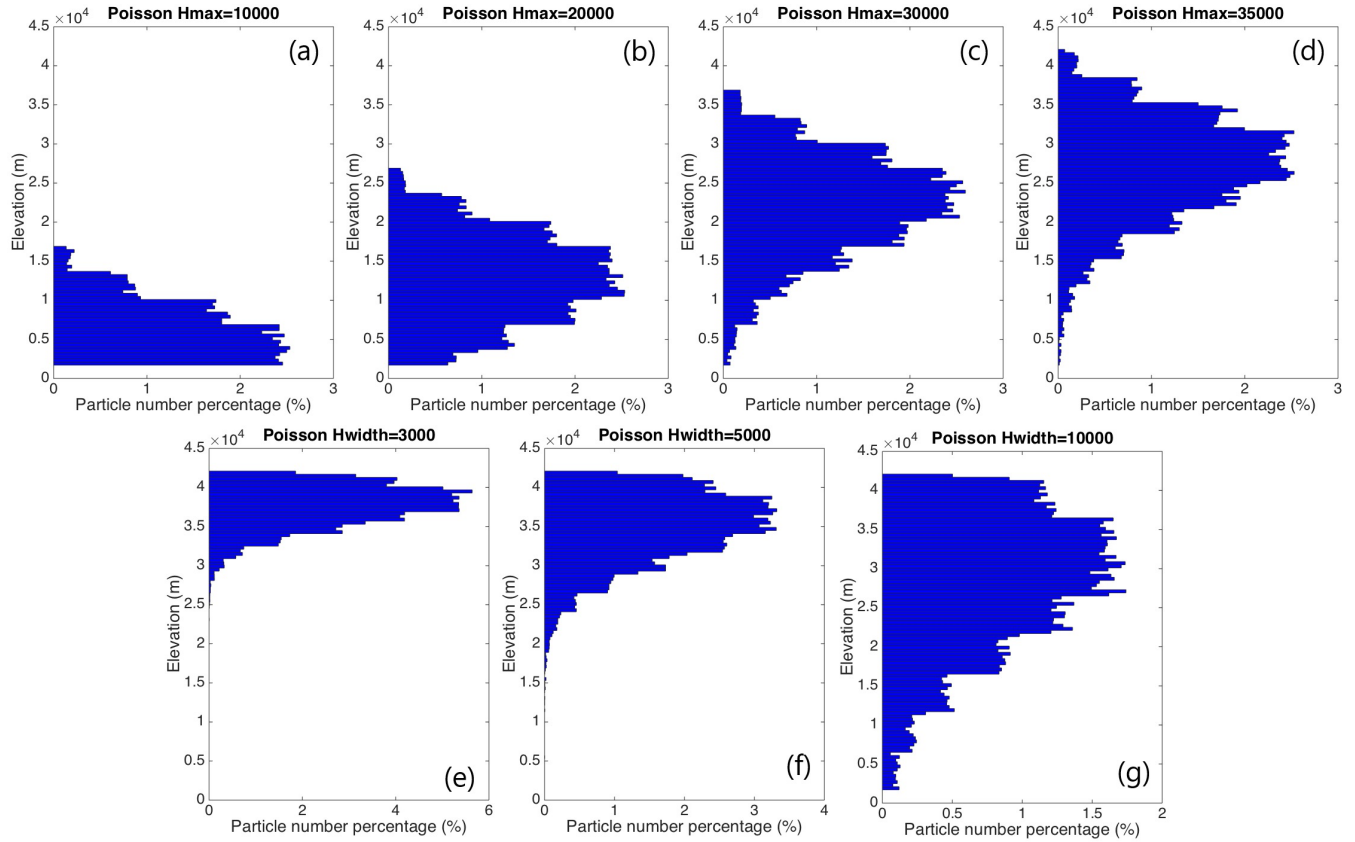


**Figure 8.** Initial particle distribution in vertical direction based on Poisson plume shape (Eq. (13)). The first row varies plume heights. (a) to (d) are corresponding to plume height of 10 km, 20 km, 30 km, 35 km. Another parameter,  $H_{width}$  is 6662 m for all four figures in the first row. The second row varies “vertical spread”,  $H_{width}$ . (e) to (g) are corresponding to vertical spread of 3 km, 5 km and 10 km. The plume height,  $H_{max}$  is set to 40 km for all three figures. The  $x$  axis is the percentage of particle numbers. See Fig. 7 for vertical ash distribution of Plume-SPH output.

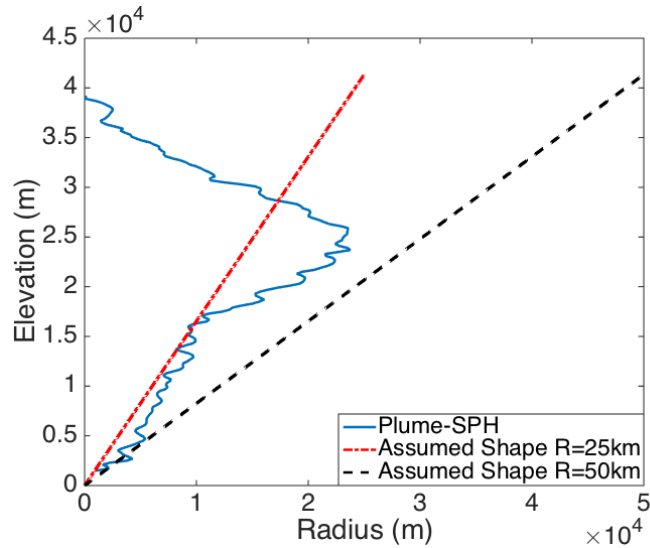


**Figure 9.** Comparison between radius of initial ash clouds created by 3D plume model (Plume-SPH) and assumed initial ash cloud shape (Eq. 15) in Puff. The plume shape expression used in Puff defines an inverted cone whose actual shape changes when “horizontal spread” takes different values.  $R = 25$  km is corresponding to “horizontal spread” equals to 50 km.  $R = 50$  km is corresponding to “horizontal spread” equals to 100 km

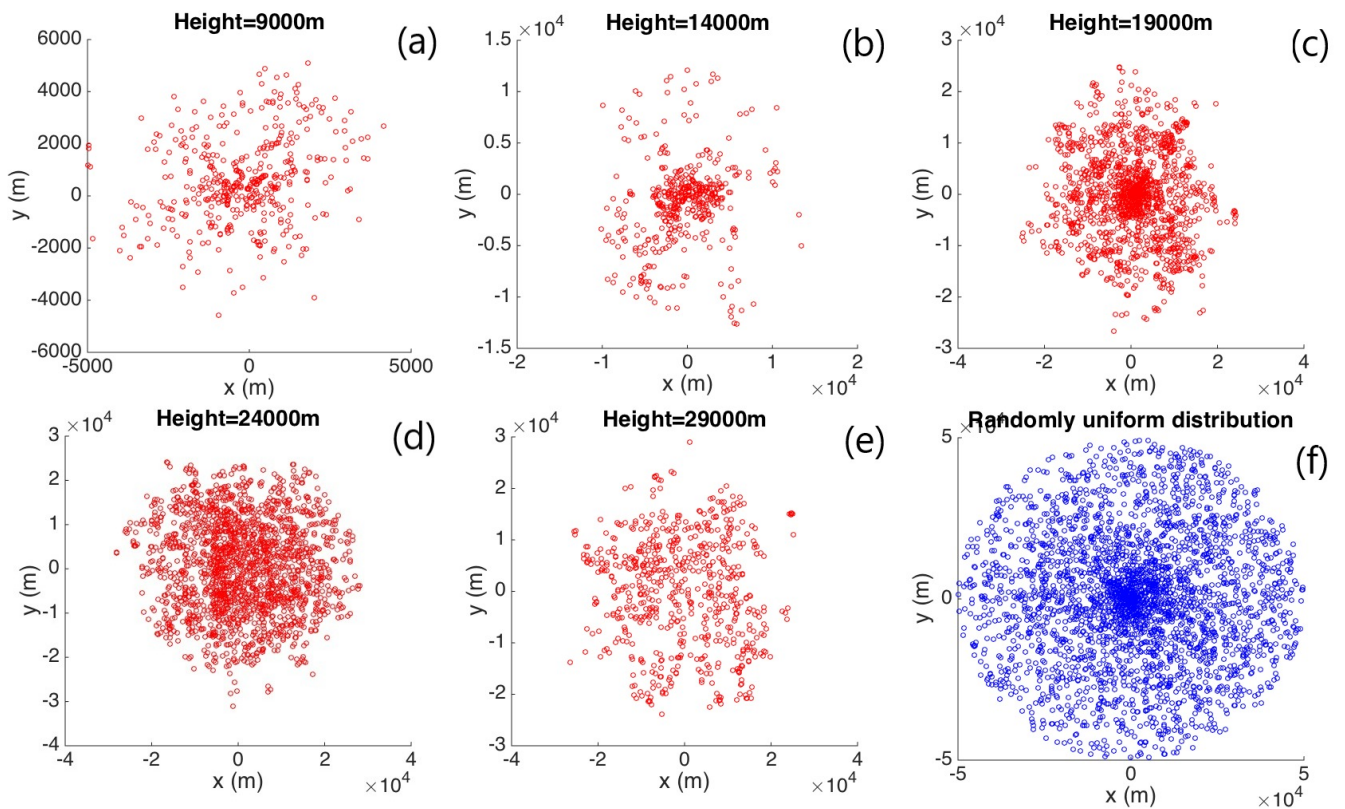


**Figure 10.** Horizontal distribution of ash particles (tracers) on a cross section of initial ash cloud. Puff assumes a randomly uniform distribution of ash particles within a circle, as shown by blue dots in (f). All other figures show the ash particle distribution of initial ash clouds created by Plume-SPH at different elevations.

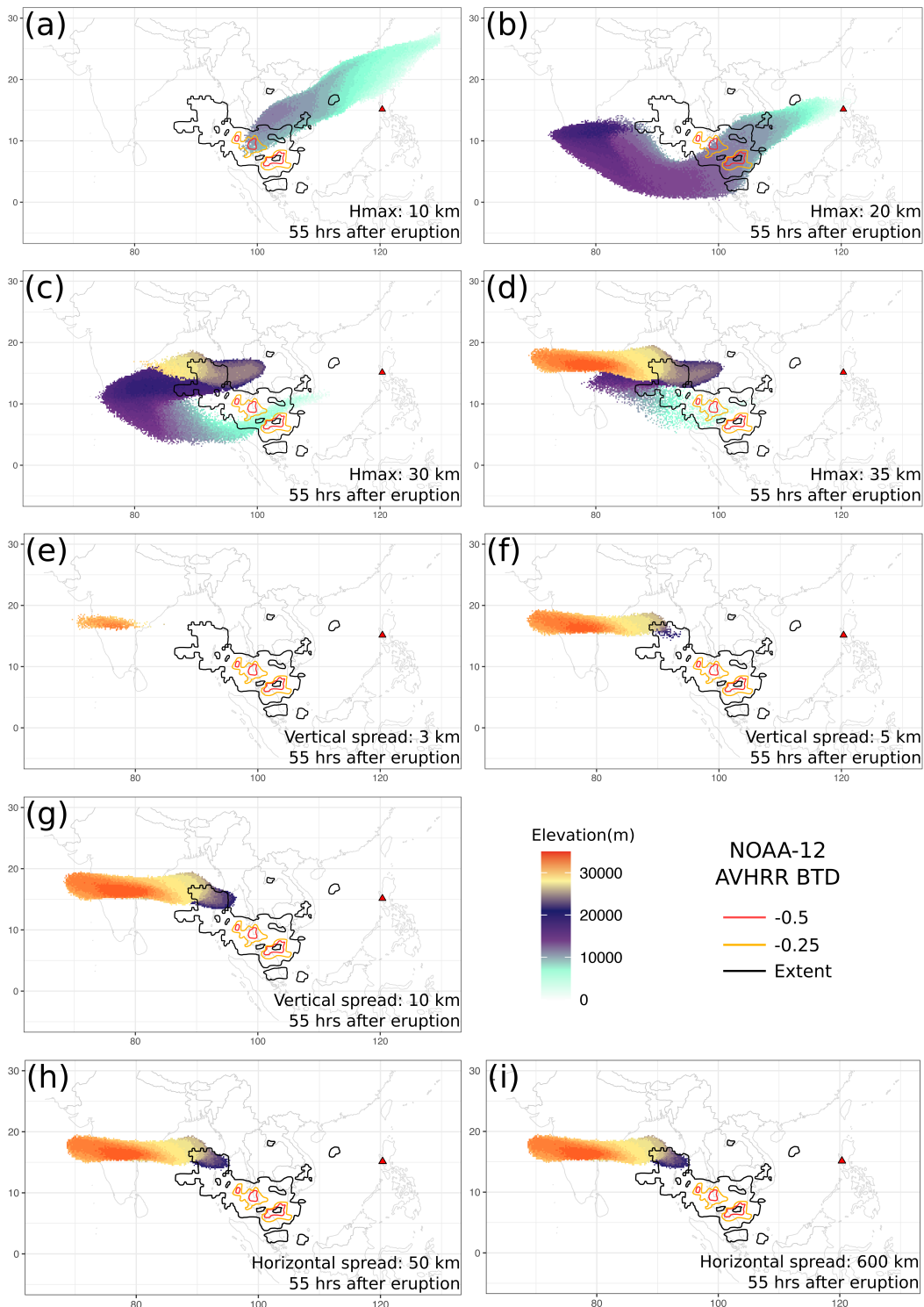


**Figure 11.** Ash transport simulated by Puff using different initial ash clouds created according the empirical expressions using different input parameters. All images are corresponding to 55 hours after eruption (UT 199106171141). More details are in the table below

Parameter	$H_{max}$				$H_{width}$			$r_{max}$	
	10 km (a) FMS	20 km (b) 0.121	30 km (c) 0.142	35 km (d) 0.227	3 km (e) 0	5 km (f) 0.039	10 km (g) 0.085	50 km (h) 0.073	600 km (i) 0.074

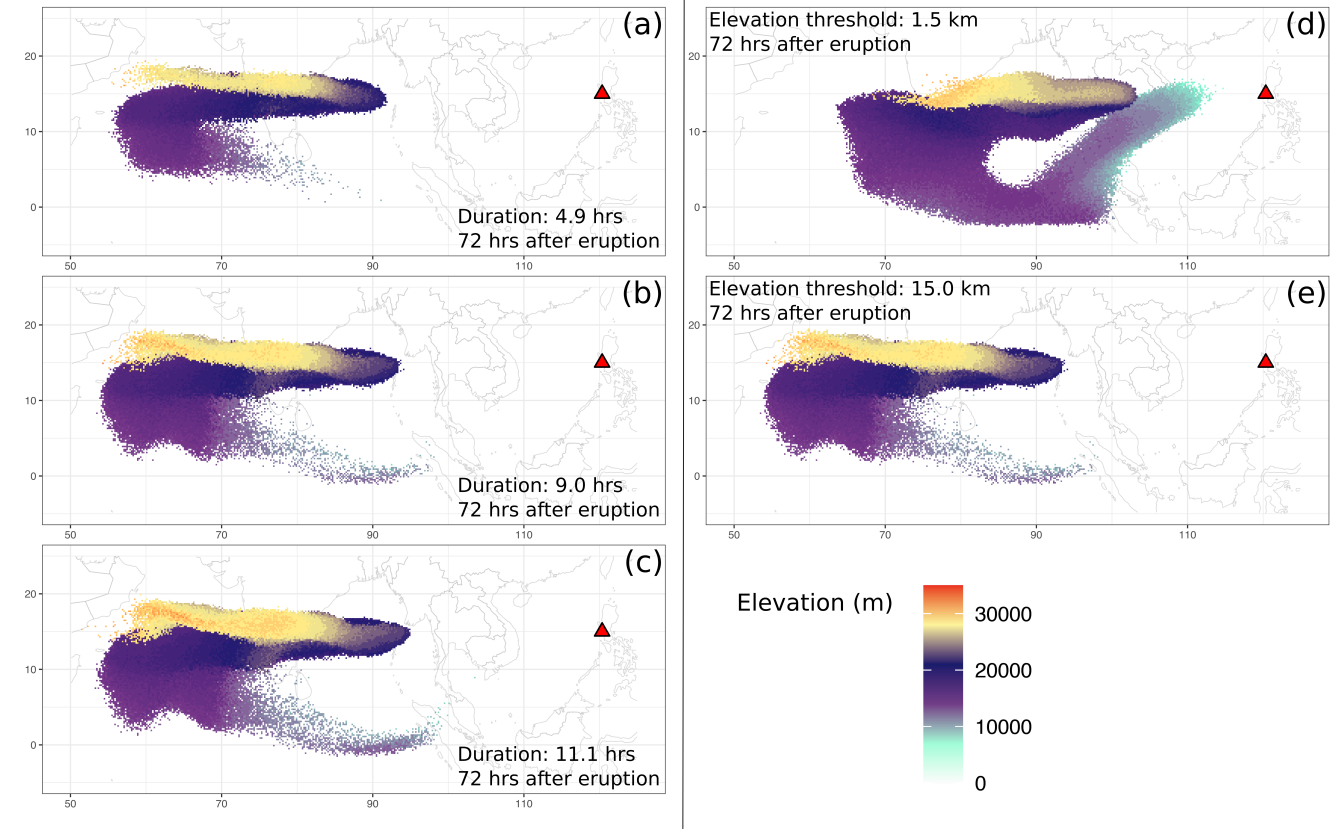


**Figure 12.** Sensitivity of Puff simulation with respect to eruption durations and initial ash cloud cutoff heights (elevation threshold). For different eruption durations, the starting and ending time for each case is in Table 3. The contours correspond to ash concentration at 72 hours after eruption. Details are in the table below.

Parameter	Eruption Duration			Elevation Threshold	
Value	4.9 hour	9 hour	11.1 hour	1500 m	15 km
Plot	(a)	(b)	(c)	(d)	(e)